Enhancing the decomposition of refractory contaminants on SO_4^{2-}-functionalized iron oxide to accommodate surface $SO_4^{\cdot-}$ generated via radical transfer from $^{\cdot}OH$

Jongsik Kim[a,*], Yun Jeong Choe[a], Sang Hoon Kim[a,b], Keunhong Jeong[c]

[a] Materials Architecting Research Center, Korea Institute of Science and Technology, Seoul, 02792, South Korea
[b] Department of Nano & Information Technology in Korea Institute of Science and Technology (KIST) School, University of Science and Technology (UST), Daejeon, 34113, South Korea
[c] Department of Chemistry, Korea Military Academy, Seoul, 01805, South Korea

ABSTRACT

$^{\cdot}OH$ or $SO_4^{\cdot-}$ are powerful oxidants that efficiently degrade recalcitrant contaminants. The productions of $^{\cdot}OH$ and $SO_4^{\cdot-}$ via activation of their precursors (H_2O_2 and $Na_2S_2O_8$), however, can be sustainable only after continuously feeding such precursors into the activators. Motivated by the advantages of $SO_4^{\cdot-}$ over $^{\cdot}OH$ as an environmental cracker, this study highlighted a simple and proficient way to persist solid-supported $SO_4^{\cdot-}$ species used to accelerate the decomposition of recalcitrants in the presence of an electric potential. While using ubiquiotous iron oxide as a platform to accomodate $SO_4^{\cdot-}$, we functionalized iron oxide surface with SO_4^{2-} species, which could be transformed into surface $SO_4^{\cdot-}$ species via radical transfer from aqueous $^{\cdot}OH$ species. Specifically, a series of SO_4^{2-}-modified iron oxide catalysts were synthesized using SO_2 and O_2 at 300–600 °C in order to vary their surface properties such as the contents of surface $Fe^{\delta+}$ species acting as H_2O_2 activators to form $^{\cdot}OH$, the contents of surface SO_4^{2-} species functioning as surface $SO_4^{\cdot-}$ precursor, and the character of S—O bonds innate to SO_4^{2-} functionalities linked to their long-term stability. In addition to the comparison of energetics between SO_4^{2-} functionalities and their $SO_4^{\cdot-}$ analogues via computation, a kinetic assessment of reaction runs were conducted under controlled environments to gather convincing evidence that the formation of surface $SO_4^{\cdot-}$ via its radical interconversion with aqueous $^{\cdot}OH$ was highly plausible and that surface $SO_4^{\cdot-}$ would be the major decomposer of phenol (model compound of recalcitrants). In addition, 500 °C was found to be the optimized temperature to greatly populate $Fe^{\delta+}$ and SO_4^{2-} species rigidly immobilized on iron oxide surface among all temperatures studied, thereby providing the greatest activity and recyclability to degrade phenol.

1. Introduction

Advancing radical-assisted oxidative degradation of aqueous pollutants is oftentimes limited by finite activators to sustainably excite radical precursors, leading to the production of abundant radical resources (e.g., H_2O_2 activated to form $^{\cdot}OH$) [1–11]. This limitation arouses the need to develop a solid, wherein sufficient amount of activators are populated, are of considerable tolerance to the leaching of activators, and thus efficiently catalyze H_2O_2 scissions in a heterogeneous manner [1–11].

Iron oxide is deemed as a cheap, ubiquitous platform that affords a wide spectrum of surface species including $Fe^{\delta+}$ activators (i.e., $Fe_{HETERO}^{\delta+}$, $\delta \leq 2$ in Fig. 1 (b)) that outperform their Fe^{3+} analogues for

H_2O_2 cleavage (Fe_{HETERO}^{3+} in Fig. 1) [1–4]. Iron oxide, however, fails to resist the leaching of Fe species when pH conditions are < 5 [1–4]. Albeit the leached, unsupported $Fe^{\delta+}$ species are active to generate $^{\cdot}OH$ via homogeneous catalysis ($Fe_{HOMO}^{\delta+}$ in Fig. 1 (a)), this reaction leads to the production of Fe^{3+} counterparts reported as sluggish activators to cleave H_2O_2 (Fe_{HOMO}^{3+} in Fig. 1) [1–4]. Unless an abundant quantity of electrons (e-) was fed, Fe_{HOMO}^{3+} could be hardly reduced to form $Fe_{HOMO}^{\delta+}$, thereby acting as a 'sink' to quench catalytic H_2O_2 scission [1–4]. Of note, $Fe^{\delta+}$ or Fe^{3+} species located underneath the surface can be exposed to H_2O_2 after $Fe_{HETERO}^{\delta+}$ and Fe_{HETERO}^{3+} species are leached from the surface ($Fe_{ADD}^{\delta+}$ and Fe_{ADD}^{3+} in Fig. 1) [1–4]. However, a limited amount of $Fe_{ADD}^{\delta+}$ species can find themselves scarcely deployed as activators to excite H_2O_2 species and therefore barely detour to reduce the lifetime of

$$H_2O_2 + e^- \text{ from } Fe^{\delta+}_{HOMO} \rightarrow {}^\bullet OH + OH^- + Fe^{3+}_{HOMO}$$
$$Fe^{3+}_{HOMO} + e^- \rightarrow Fe^{\delta+}_{HOMO} \quad \ddagger \qquad \textbf{(a)}$$

$$SO_4^{2-} + {}^\bullet OH + H^+ \rightarrow SO_4^{\bullet-} + H_2O$$
$$SO_4^{2-} + {}^\bullet OH \rightarrow SO_4^{\bullet-} + OH^-$$
$$SO_4^{\bullet-} + e^- \rightarrow SO_4^{2-} \qquad \textbf{(d)}$$

$$Fe\text{-}SO_3^{2-}$$

$$Fe^{\delta+}_{HOMO} \qquad Fe^{3+}_{HOMO}$$

$$SO_4^{2-} \qquad Fe\text{-}SO_4^{2-} \qquad Fe^{3+}_{ADD} \qquad Fe^{\delta+}_{ADD}$$

$$Fe^{3+}_{HETERO} \qquad Fe^{\delta+}_{HETERO}$$

$$Fe\text{-}SO_4^{2-} + {}^\bullet OH + H^+ \rightarrow Fe\text{-}SO_4^{\bullet-} + H_2O$$
$$Fe\text{-}SO_4^{2-} + {}^\bullet OH \rightarrow Fe\text{-}SO_4^{\bullet-} + OH^-$$
$$Fe\text{-}SO_4^{\bullet-} + e^- \rightarrow Fe\text{-}SO_4^{2-} \qquad \textbf{(c)}$$

$$H_2O_2 + e^- \text{ from } Fe^{\delta+}_{HETERO} \text{ (or } Fe^{\delta+}_{ADD}) \rightarrow {}^\bullet OH + OH^- + Fe^{3+}_{HETERO} \text{ (or } Fe^{3+}_{ADD})$$
$$Fe^{3+}_{HETERO} \text{ (or } Fe^{3+}_{ADD}) + e^- \rightarrow Fe^{\delta+}_{HETERO} \quad \ddagger \qquad \textbf{(b)}$$
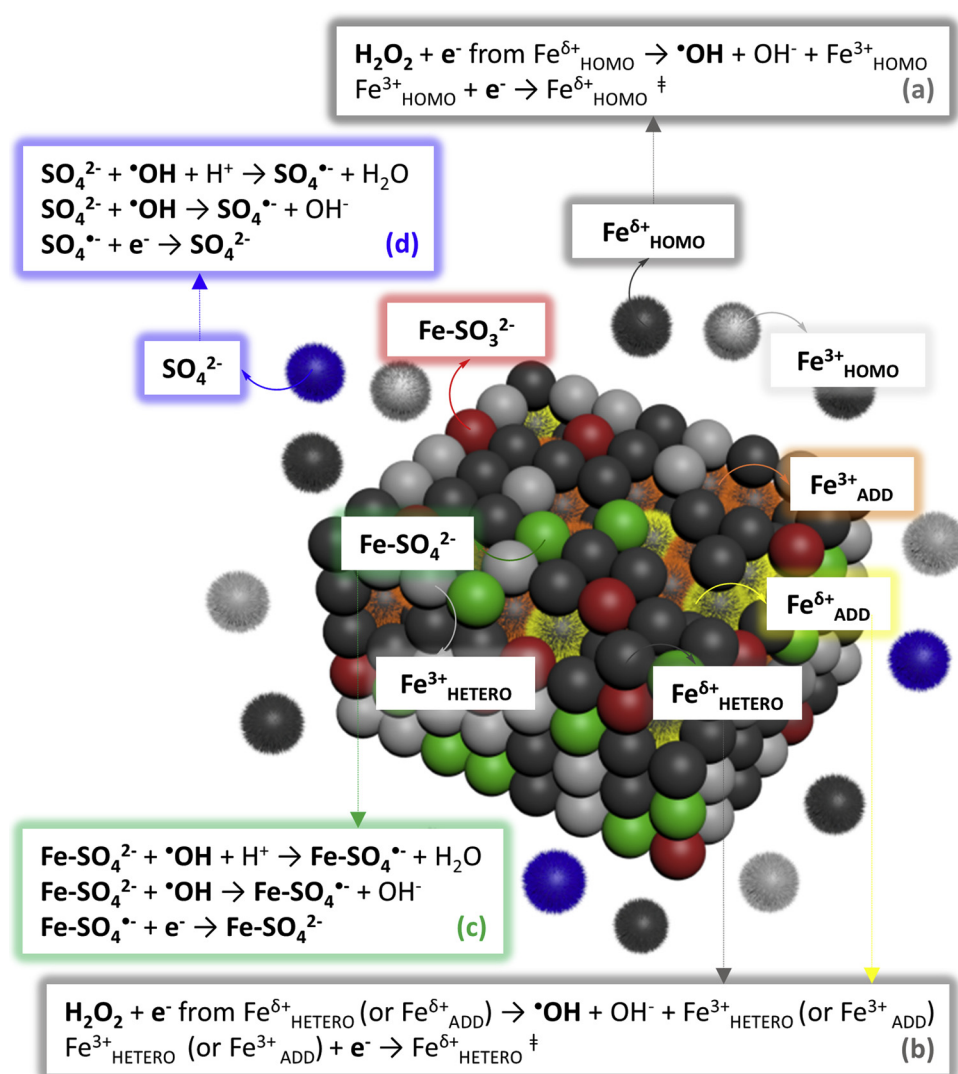
Fig. 1. Illustration of SO_4^{2-}-functionalized iron oxide active to produce ${}^\bullet OH$ or $SO_4^{\bullet-}$ via different pathways. Generation of ${}^\bullet OH$ on (a) leached $Fe^{\delta+}$ ($\delta \leq 2$) via homogeneous catalysis ($Fe^{\delta+}_{HOMO}$) or on (b) supported $Fe^{\delta+}$ via heterogeneous catalysis ($Fe^{\delta+}_{HETERO}$ or $Fe^{\delta+}_{ADD}$). Generation of $SO_4^{\bullet-}$ on (c) supported $Fe\text{-}SO_4^{2-}$ or on (d) leached SO_4^{2-}. O atoms and elementary steps to describe $SO_4^{\bullet-}$ generation on leached $Fe\text{-}SO_4^{2-}$ are omitted for simplicity. e- denotes electron, whereas $Fe^{\delta+}_{ADD}$ and Fe^{3+}_{ADD} denote Fe species exposed to H_2O_2 post surface Fe leaching. $Fe\text{-}SO_3^{2-}$ and Fe^{3+} present on or near the surface are also exhibited (*i.e.*, Fe^{3+}_{HETERO} and Fe^{3+}_{HOMO}).

iron oxide acting as a shuttle for activators [1–4].

To evade the issues of iron oxide stated above, its O-modified $Fe^{\delta+}$ activators experienced structural/electronic modification by sulfur (S) through the formation of S-doped iron oxide [12–14] or FeS_2/Fe_7S_8 [15–17]. The resulting, S-modified $Fe^{\delta+}$ species were validated to enhance H_2O_2 scission rate and conversion over their O-modified $Fe^{\delta+}$ counterparts [12,16,17]. This was responsible for their Lewis acidities adequate to interact with and turnover H_2O_2 [15] or facilitated intermolecular e- transfer between H_2O_2 and S-modified $Fe^{\delta+}$ species [17,18]. S-modified $Fe^{\delta+}$ species, however, aggravated their H_2O_2 activation performance throughout their recycled utilization [12,16,17]. This potentially resulted from the persistent leaching of surface $Fe^{\delta+}$ species even at near-neutral pH conditions combined with the oxidation of surface $Fe^{\delta+}$ species by ${}^\bullet OH$ to produce Fe^{3+} adducts [12–19]. Therefore, it is highly convincing that a consistent decrease in H_2O_2 scission consequence caused by $Fe^{\delta+}$ leaching appears inevitable in most Fe-bearing solids [1–4,12–19].

To minimize the repercussions caused by the liberation of $Fe^{\delta+}$ species from Fe-bearing surfaces [1–4,12–19], here we propose an interesting synthetic strategy to functionalize iron oxide surface with SO_4^{2-} species. Advantages of $SO_4^{\bullet-}$ relative to ${}^\bullet OH$ establish the basis for this work such as longer lifetime in an aqueous medium and easier generation over a broad pH range, in spite of greater oxidation power of ${}^\bullet OH$ in comparison with $SO_4^{\bullet-}$ (i.e., standard oxidation potential of ~2.6 eV for $SO_4^{\bullet-}$; ~2.8 eV for ${}^\bullet OH$) [20–24]. We conjecture that SO_4^{2-}

present in the surface of iron oxide can be converted into $SO_4^{\bullet-}$ via radical subtraction from ${}^\bullet OH$ ($Fe\text{-}SO_4^{2-}$ in Fig. 1). This type of radical transfer is particularly fascinating when taking into account the shortcomings of HSO_5^- or $S_2O_8^{2-}$ excitation on $Fe^{\delta+}$ species, during which control over the pH value is essential in addition to taking risks that $SO_4^{\bullet-}$ participates in the oxidation of $Fe^{\delta+}$ to form Fe^{3+} [12,13,19,25].

Our hypotheses mentioned above, however, can be efficiently realized only after a large number of ${}^\bullet OH$ radicals are populated vicinal to SO_4^{2-} functionalities on the surface of iron oxide. For this reason, a (pseudo) electro-Fenton reaction system served in this study. This was because of two potential benefits expected from the use of such a reaction system as to produce abundant ${}^\bullet OH$ precursors (H_2O_2) on the cathode ($2H^+ + O_2 + 2e^- \rightarrow H_2O_2$) and to recover Fe^{3+} to $Fe^{\delta+}$ via e- reduction on the cathode in the presence of an electric potential ($\ddagger$ in Fig. 1 (a) and 1 (b)) [24,26,27]. In this reaction system, a graphite anode was reported to boost two H_2O oxidation pathways such as '$H_2O \rightarrow {}^\bullet OH + H^+ + e^-$' and '$2H_2O \rightarrow O_2 + 4H^+ + 4e^-$' [24,28]. Of note, the resulting ${}^\bullet OH$ product could react with the surface of the graphite anode, leading to the formation of chemisorbed O species active to degrade aqueous contaminants (denoted as anodic oxidation) [24,28]. Conversely, H^+ and O_2 could migrate into cathode and undergo O_2 reduction to form H_2O_2 ($2H^+ + 2e^- + O_2 \rightarrow H_2O_2$) [24,26,27]. H_2O_2 was subsequently activated by $Fe^{\delta+}$ of iron oxide coated on the cathode to ultimately yield ${}^\bullet OH$ (Fig. 1 (a) and 1 (b)) [24,26,27]. Of additional note, the quantity of e- might be sufficient to keep reducing unleached

Fe^{3+} species to recover $Fe\delta^+$ activators ($Fe\delta^+_{HETERO}$ or $Fe^{\delta+}_{ADD}$), which could be utilized for the sustainable production of ˙OH post the continuous evolution of H_2O_2. Therefore, it was presumed the reduction of supported Fe^{3+} by e- might compensate for the continuous and unavoidable loss of $Fe^{\delta+}$ activators, which is detrimental to sustain ˙OH productivity.

During electro-Fenton runs, ˙OH was hypothesized to experience radical interconversion with $Fe-SO_4^{2-}$ to form $Fe-SO_4$˙- in the presence of H_2O oxidation-driven H^+ species (Fig. 1 (c)). Of note, two pathways to transfer radicals from SO_4˙- to ˙OH were reported to be of great favor with reaction rate constants of 660 s^{-1} for SO_4˙- + $H_2O \rightarrow SO_4^{2-}$ + ˙OH + H^+ at all pH values and ~10^8 M^{-1} s^{-1} for SO_4˙- + OH- $\rightarrow SO_4^{2-}$ + ˙OH at basic pH values [20,29–31]. Our reaction system, however, included SO_4^{2-} species bound to the surface of iron oxide and might provide significant amounts of ˙OH and H^+. These might change the dynamics of these reactions and thus might reverse them, as depicted in Fig. 1 (c) and (d).

In order to validate all assumptions discussed above, we synthesized a series of porous, SO_4^{2-}-functionalized iron oxide catalysts with the use of SO_2 and O_2 at elevated temperatures. Temperature was set as a major synthetic parameter and was varied from 300 to 600 °C. We found these temperatures can greatly affect the distributions of surface $Fe^{\delta+}$ and SO_4^{2-} species in conjunction with the feature of S−O bonds innate to SO_4^{2-} functionalities, as was also observed in our previous studies on $Cu_3V_2O_8$ or $Fe_2V_4O_{13}$ on TiO_2 catalysts [32–34]. The resulting catalysts were extensively characterized and examined to decompose a model compound of recalcitrant contaminants, phenol [15,35–37]. The reaction environments were also regulated to verify whether the reaction pathways shown in Fig. 1(b) and (c) are feasible, recyclable, and to identify the roles of ˙OH and $Fe-SO_4$˙- during phenol degradation.

2. Experimental and computational

2.1. Synthesis of catalysts

Iron oxide catalysts were synthesized using a procedure that was slightly modified from those in our previous reports [14,32,33]. Typically, 20 mmol of oxalic acid ($C_2H_2O_4$·$2H_2O$, Sigma-Aldrich, ≥99.0%) dissolved in 50 mL of de-ionized H_2O was stirred at 50 °C for 30 min before adding 20 mmol of $FeSO_4$·$7H_2O$ (Sigma-Aldrich, ≥99.0%) dissolved in 50 mL of de-ionized H_2O [14]. The resulting synthetic mixture was stirred for 30 min, cooled to room temperature, and vacuum-filtered using 500 mL of de-ionized H_2O and 500 mL of ethanol (C_2H_5OH, DAEJUNG, 94.5%) to collect yellow precipitate [14]. The precipitate was dried at 70 °C overnight, calcined at 300 °C for an hour with a ramping rate of 4 °C min^{-1}, and cooled to room temperature [14]. This led to the formation of iron oxide. Iron oxide (pristine) was then subjected to surface functionalization with SO_4^{2-} species at 300, 400, 500, or 600 °C for an hour with a ramping rate of 10 °C min^{-1} [32,33]. 500 ppm of SO_2 combined with 3 vol. % O_2 were utilized as a precursor for SO_4^{2-} functionalities on the surface of iron oxide, whereas N_2 served as a balance gas for setting the total flow rate of 500 mL min^{-1} [32,33]. The resulting SO_4^{2-}-modified iron oxide catalyst was cooled to room temperature under a N_2 atmosphere prior to its utilization.

2.2. Characterizations

X-ray diffraction (XRD) patterns of the catalysts were collected on D8 Advance (Bruker) with the use of monochromatic Cu K_α radiation (λ = 1.54 Å) at a scan speed of 2 s per step and a step size of 0.02° per step. The crystallite sizes of the catalysts at (113) or (024) planes were evaluated using the Scherrer equation (Equation (1)), where K, β, and θ indicates the shape factor (0.89), the line broadening at half the maximum intensity, and the Bragg angle for the (113) or (024) planes [38].

$$d = \frac{\kappa \times \lambda}{\beta \times \cos \theta} \tag{1}$$

X-ray fluorescence (XRF) analysis of the catalysts was carried out using ZSX Primus II (Rigaku) to quantify their bulk Fe and S contents. The porosity of the catalysts was analyzed via N_2 physisorption with the use of ASAP 2010 (Micromeritics) at 77 K. X-ray photoelectron (XP) spectroscopy analysis of the catalysts was performed using PHI 5000 VersaProbe, Adventitious carbon with a binding energy of 284.6 eV was used as a reference to correct binding energies of Fe and S species present in the surfaces of the catalysts. High resolution transmission electron microscopy (HRTEM) images and selected area electron diffraction (SAED) patterns of the catalysts were collected using Titan 80–300 TM (FEI) at 300 keV. Scanning electron microscopy images of the catalysts were collected using Inspect F51 (FEI) at 10 kV. CO-pulsed chemisorption analysis of the catalysts was performed using Autochem II (Micromeritics) to quantify their CO-accessible sites at 40 °C [39–41]. in situ diffuse reflectance Infrared Fourier transform (DRIFT) spectroscopy analysis of the catalysts was carried out using FT/IR/4200 (Jasco) [32,33]. The catalyst was situated inside a reaction cell (Harrick Scientific), purged at 300 °C for an hour under a 3 vol. % O_2/N_2 before changing its temperature to 50 °C or 300–500 °C under a N_2 atmosphere to collect background spectrum of the catalyst [32,33]. Background-subtracted, in situ DRIFT spectrum of the catalyst was then recorded at 50 °C under a 1000 ppm NH_3/N_2 or at 300–500 °C under a 1000 ppm SO_2/3 vol. % O_2/N_2 [32,33]. N_2 was used as a balance gas for setting the total flow rate of 200 mL min^{-1} [32,33]. Inductively coupled plasma-atomic absorption spectrometry (ICP-AAS) experiments were performed on ICS 3000 (Thermo Fisher Scientific) to quantify Fe species leached from the catalysts during the reaction runs. Electric conductivities of the reaction mixtures were analyzed using HI98191 (HANNA). 2,9-dimethyl-1,10-phenanthroline ($C_{14}H_{12}N_2$, Sigma-Aldrich, ≥ 98%) method reported by K. Kosaka and co-workers was utilized to quantity the amount of hydrogen peroxide (H_2O_2) produced or consumed during the reaction runs [42]. Conversions of H_2O_2 (X_{H2O2}) were calculated using Eq. (2), in which $C_{H2O2, 0}$ and C_{H2O2} denote initial H_2O_2 concentration and H_2O_2 concentration at a specific reaction time, respectively [15]. Initial H_2O_2 activation rates in the presence of the catalysts (-$r_{H2O2, 0}$) were calculated using Equation (3), where k_{APP} denotes apparent reaction rate constant obtained through the fitting of reaction data to pseudo-1st-order kinetic model, whereas $N_{H2O2, 0}$ indicates moles of H_2O_2 initially added prior to the reaction runs [15].

$$X_{H2O2}(\%) = \frac{C_{H2O2,0}(mol\ L^{-1}) - C_{H2O2}(mol\ L^{-1})}{C_{H2O2,0}(mol\ L^{-1})} \times 100 \tag{2}$$

$$-r_{H2O2,0}(min^{-1}) = \frac{\kappa_{APP}(min^{-1}) \times N_{H2O2,0}(mol)}{0.2 g_{CAT}} \tag{3}$$

The amount of phenol (C_6H_5OH, DAEJUNG, 99%) remaining in the reaction mixture at a specific reaction time was quantified using high-performance liquid chromatography (LC-20 A, Shimadzu) [15]. Conversions of phenol (X_{PHENOL}) were calculated using Equation (4), where $C_{PHENOL, 0}$ and C_{PHENOL} indicate initial phenol concentration and phenol concentration at a specific reaction time, respectively [15]. Initial phenol degradation rates in the presence of the catalysts (-$r_{PHENOL, 0}$) were evaluated using Eq. (5). In Eq. (5), k_{APP} denotes apparent reaction rate constant obtained through the fitting of reaction data to pseudo-1st-order kinetic model, whereas $N_{PHENOL, 0}$ denotes moles of phenol initially added prior to the reaction runs [15]. Initial phenol adsorption rates in the presence of the catalysts (-$r'_{PHENOL, 0}$) were also evaluated using Eq. (6). In Eq. (6), k'_{APP} denotes apparent adsorption rate constant obtained through the fitting of adsorption data to pseudo-1st-order kinetic model, whereas $N'_{PHENOL, 0}$ denotes moles of phenol initially added prior to the adsorption runs.

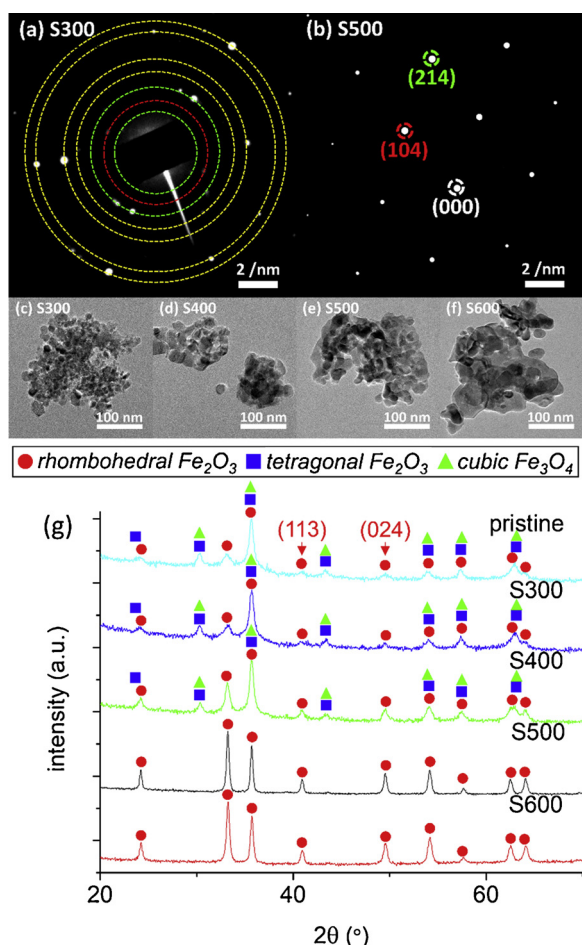**Fig. 2.** (a–b) SAED patterns of S300 and S500. In (a), red circle indicates (012) facet of *rhombohedral* α-Fe$_2$O$_3$, whereas green circles indicate crystal facets of *tetragonal* γ-Fe$_2$O$_3$ or *cubic* Fe$_3$O$_4$. Yellow circles indicate crystal facets of *rhombohedral* α-Fe$_2$O$_3$, *tetragonal* γ-Fe$_2$O$_3$, or *cubic* Fe$_3$O$_4$. In (b), dots denote diffractions of *rhombohedral* α-Fe$_2$O$_3$. (c–f) HRTEM images of SO$_4^{2-}$-functionalized catalysts. (g) XRD patterns of the catalysts (For interpretation of the references to colour in this figure legend, the reader is referred to the web version of this article).

$$X_{PHENOL}(\%) = \frac{C_{PHENOL,0}(mol\,L^{-1}) - C_{PHENOL}(mol\,L^{-1})}{C_{PHENOL,0}(mol\,L^{-1})} \times 100 \qquad (4)$$

$$- r_{PHENOL,0}(min^{-1}) = \frac{\kappa_{APP}(min^{-1}) \times N_{PHENOL,0}(mol)}{0.2g_{CAT}} \qquad (5)$$

$$- r'_{PHENOL,0}(min^{-1}) = \frac{\kappa'_{APP}(min^{-1}) \times N'_{PHENOL,0}(mol)}{0.2g_{CAT}} \qquad (6)$$

2.3. Reactions

Reactions were performed following the procedures that were slightly modified from those reported in our previous publications [15,27]. 7 g of poly (vinylidene fluoride) ((CH$_2$CF$_2$)$_n$, average M$_w$ ~180,000, average M$_n$ ~71,000, Sigma-Aldrich) was dissolved in 93 g of *N*-Methyl-2-pyrrolidone (C$_5$H$_9$NO, Sigma-Aldrich, ≥ 99%) to form a binder solution. 0.2 g of the binder solution was then mixed with 0.2 g of the catalyst, leading to the formation of a catalyst slurry. A graphite plate used as a cathode (Groupe Carbone Lorraine, grade 2124) was coated with the catalyst slurry with an area of 3 cm × 4 cm and dried overnight at 110 °C. The catalyst-coated cathode and the graphite utilized as an anode was positioned vertically with a gap of 3 cm and put

into a 150 mL beaker including the reaction solution. The reaction solution typically consisted of 100 mL of pH-neutral de-ionized H$_2$O and 0.2 mol of Na$_2$SO$_4$ electrolyte (Sigma-Aldrich, ≥ 99%) with or without H$_2$O$_2$ (Sigma-Aldrich, 29.0–32.0 wt. %, H$_2$O$_2$ basis), phenol, *iso*-propyl alcohol (C$_3$H$_7$OH, DAEJUNG, 99.5%), or *tert*-butyl alcohol (C$_4$H$_9$OH, DAEJUNG, 99.5%). The reaction was initiated by stirring the reaction solution at 300 rpm and at 25 °C with or without electric potential of 3 V (~12 mA). The content of H$_2$O$_2$ or phenol at a specific reaction time was quantified using 1 mL of reaction aliquot taken from the reaction mixture, which was quenched with 1 μL of methanol (CH$_3$OH, Sigma-Aldrich, 99.8%) and filtered over 0.45 μm sized-PES syringe filter (Whatman®). After the reaction run, the catalyst was separated from the cathode, collected through vacuum filtration, washed with 300 mL of de-ionized H$_2$O and 300 mL of ethanol, and dried overnight at 110 °C.

2.4. Computations

Thermal/electronic energy change involved during the transition of SO$_4^{2-}$ → SO$_4$·- or Fe-SO$_4^{2-}$ → Fe-SO$_4$·- was computed via cluster model using Gaussian 09 (Revision C.01) package. Prior to the calculation, H$_2$O molecules were eliminated from the surface of Fe$_2$O$_3$, whose structure was specified in previous literatures [43,44]. The structure of the Fe$_2$O$_3$ cluster was fixed during the calculation to better simulate SO$_4^{2-}$ or SO$_4$·- adsorbed on the Fe$_2$O$_3$ cluster and was relaxed/optimized prior to the energetic analysis. Since SO$_4$·- radical and its adsorption on the Fe$_2$O$_3$ were successfully described with B3LYP/6-311+G (d,p) level [45], the geometry optimization and vibrational frequencies for all the structures were calculated using the identical level of theory along with LanL2DZ for describing Fe atoms.

3. Results and discussion

3.1. Catalysts

Iron oxide was synthesized with the use of oxalate as a pore directing/precipitating agent, which was eliminated through the calcination of ferrous oxalate intermediate (FeC$_2$H$_4$), while leaving iron oxide [14]. To functionalize iron oxide surface with SO$_4^{2-}$, iron oxide was subsequently exposed to SO$_2$ and O$_2$ at such temperatures that could dynamically alter the properties of SO$_4^{2-}$-modified iron oxide surface such as 300, 400, 500, and 600 °C. This led to the formation of SXXX, where XXX denotes the temperature utilized to modify iron oxide surface. Notably, our choice of this synthetic method was because of its benefit to highly disperse Fe$^+$ and SO$_4^{2-}$ species throughout porous iron oxide surface [14,32,33], thus favoring the generation of ·OH and SO$_4$·-.

The X-ray diffraction (XRD) patterns of the catalysts were used to investigate their phases and crystallite sizes, whereas these were further elaborated by selected area electro diffraction (SAED) patterns and high resolution transmission electron microscopy (HRTEM) images of the catalysts (Fig. 2). XRD patterns of pristine, S300, and S400 showed crystal facets that could be assigned to *rhombohedral* α-Fe$_2$O$_3$, *tetragonal* γ-Fe$_2$O$_3$, or *cubic* Fe$_3$O$_4$ (Fig. 2 (g)). Such overlaps were also observed in the SAED patterns of these catalysts, which showed that their surfaces comprised of multiple crystal planes assigned to α-Fe$_2$O$_3$, γ-Fe$_2$O$_3$, or Fe$_3$O$_4$, as shown in Fig. 2 (a) (SAED patterns of pristine/S400 and S600 are omitted due to their crystallographic similarity to S300 and S500, respectively.) Conversely, the catalysts functionalized with SO$_4^{2-}$ at > 400 °C experienced oxidative phase transition of γ-Fe$_2$O$_3$ or Fe$_3$O$_4$ to stable α-Fe$_2$O$_3$, which was accelerated at high temperatures, as reported elsewhere [46,47]. Indeed, S500 and S600 missed two major diffractions of γ-Fe$_2$O$_3$ or Fe$_3$O$_4$ located at 2θ values of ~30° ((206) for γ-Fe$_2$O$_3$; (220) for Fe$_3$O$_4$) and ~43° ((00 12) for γ-Fe$_2$O$_3$; (400) for Fe$_3$O$_4$) in their XRD patterns. This was in close accordance with the SAED patterns of S500 and S600, both of which only exhibited diffraction peaks corresponding to those of α-Fe$_2$O$_3$ (Fig. 2 (b)). Scherrer equation

also served to calculate the crystallite sizes of α-Fe$_2$O$_3$ innate to the catalysts at the (113) and (024) facets. α-Fe$_2$O$_3$ crystallite sizes were larger in the catalysts, whose surfaces were functionalized with SO$_4^{2-}$ at higher temperatures (S300→S600; ˜14.7 nm→˜58.8 nm on (113); ˜12.8 nm→˜58.5 nm on (024)). This could result from growth of iron oxide crystallites via Ostwald ripening at elevated temperatures [48,49] and could be further corroborated by the HRTEM images of the catalysts. All catalysts were composed of iron oxide poly-crystallites aggregated to form large particles in the sizes of 100–700 nm, as shown in Fig. 2 (c)-(f). (SO$_4^{2-}$-unmodified Fe$_2$O$_3$ is omitted due to its morphological similarity to S300.) 5–20 nm-sized iron oxide crystallites found in pristine and S300, however, were greatly agglomerated at SO$_4^{2-}$ functionalization temperatures of ≥ 400 °C. This led to the formation of 30–100 nm sized iron oxide chunks post SO$_4^{2-}$ functionalization of the catalyst at 600 °C (Fig. 2 (f)).

N$_2$ physisorption experiments of the catalysts were then performed for the observation of their textural properties. Pristine exhibitd the largest porosity among the catalysts (Brunauer-Emmett-Teller surface area (S$_{BET}$) of ˜170 m^2 g$_{CAT}^{-1}$; Barrett- Joyner-Halenda pore volume (V$_{BJH}$) of ˜0.3 cm^3 g$_{CAT}^{-1}$). On the other hand, S300-S600 revealed reduced porosities, which could originate from the surface SO$_4^{2-}$ functionalities occupying the pores of iron oxide [32,33]. Such a decrease in the porosities of S300-S600 was more pronounced to those with SO$_4^{2-}$-modification at greater temperatures, which again potentially originated from the aggregation of iron oxide poly-crystals observed in HRTEM images of the catalysts (S300→S600; S$_{BET}$ of ˜130 m^2 g$_{CAT}^{-1}$→ ˜20 m^2 g$_{CAT}^{-1}$; V$_{BJH}$ of ˜0.3 cm^3 g$_{CAT}^{-1}$→˜0.1 cm^3 g$_{CAT}^{-1}$) [48,49].

X-ray photoelectron (XP) spectroscopy was then used to better understand the traits of surface Fe species innate to the catalysts. Their XP spectra showed two broad bands in Fe 2p$_{3/2}$ regimes (Fig. 3 (a)). These were de-convoluted into three sub-bands, among which sub-bands with binding energies centered at 709.8–710.5 eV and 711.3–712.2 eV were assigned to surface Fe$^{δ+}$ and Fe^{3+}, respectively [14,15,33,50–52]. S400 and S500 provided more abundant Fe$^{δ+}$ species (≥ ˜32.6%) than the other catalysts (≤ ˜25.7%) and thus could potentially improve productivities of ·OH used to convert SO$_4^{2-}$ to SO$_4$·-. This was indeed plausible when Lewis-acidic, CO-accessible Fe$^{δ+}$ species included per gram of the catalysts (N$_{CO}$) were quantified via CO-pulsed chemisorption experiments at 40 °C [15,33,40]. S400 and S500 showed larger N$_{CO}$ values (≥ ˜2.6 μmol$_{CO}$ g$_{CAT}^{-1}$) in comparison with the other catalysts (≤ ˜1.7 μmol$_{CO}$ g$_{CAT}^{-1}$).

Furthermore, *in situ* diffuse reflectance infrared Fourier transform (DRIFT) experiments were also performed to determine which catalyst could provide the greatest number of Lewis acidic Fe$^{δ+}$ species accessible to NH$_3$ [32,33]. (Details are found in Materials and Method section.) Background-subtracted, *in situ* DRIFT spectra of the catalysts post the saturation of their surfaces with NH$_3$ at 50 °C showed a bunch of bands (Fig. 3 (b)) [32,33]. These bands gave rise to vibrations of N−H bonds inherent to NH$_3$ interacting with the surface species with Brönsted (***B***, −OH) or Lewis acidic character (***L***, Fe$^{δ+}$) [32,33]. Interestingly, the *in situ* DRIFT spectrum of S400 showed ***L*** bands with reduced intensities, which were even smaller than those observed in the *in situ* DRIFT spectrum of S600. This could be ascribed to the nature of the Fe$^{δ+}$ species included in S300-S600, which might interact with probe molecules in a distinct manner (*e.g.*, CO and NH$_3$) [32,33]. S500, however, exhibited the largest area under the ***L*** bands, which suggested the highest ·OH productivity of S500 among all catalysts.

In addition, bulk S compositions of S300-S600 were analyzed via X-ray fluorescence (XRF). The catalysts exhibited decreased bulk S contents after their surfaces were functionalized with SO$_4^{2-}$ at higher temperatures (S300→S600; ˜0.5 mmol$_S$ g$_{CAT}^{-1}$→˜0.1 mmol$_S$ g$_{CAT}^{-1}$). S500, however, afforded the largest S content per unit surface area among all the catalysts (˜6.1 μmol$_S$ m^{-2} for S500; ≤ ˜5.3 μmol$_S$ m^{-2} for the others). Surface S concentrations of the catalysts were also investigated via XP spectroscopy. To better quantify how many surface Fe species were modified by S species in a specific catalyst, the surface S
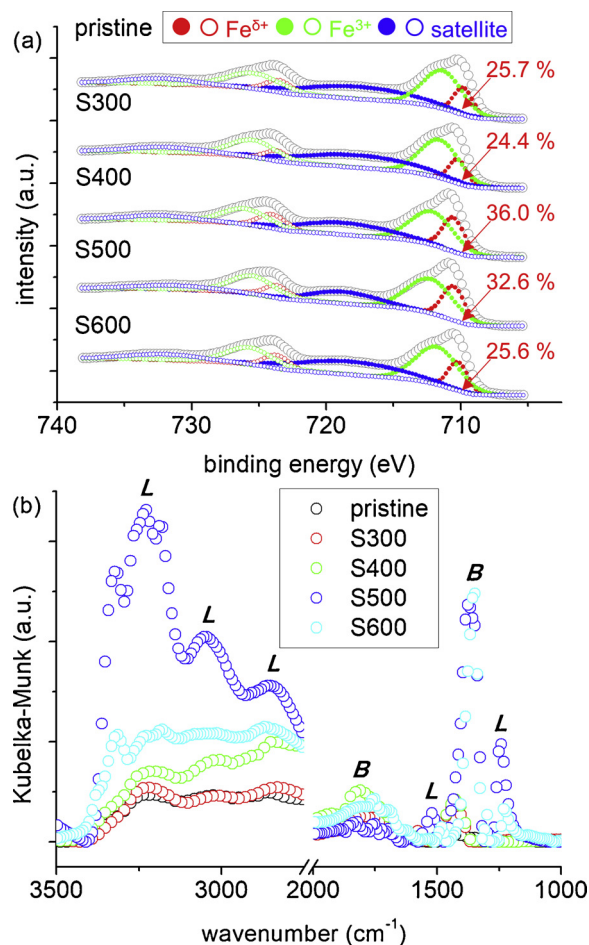

Fig. 3. (a) Fe 2p regions of XP spectra for the catalysts. In (a), grey, empty circles indicate fitted XP bands of the catalysts, wherein circles indicate surface Fe species (filled located at Fe 2p$_{3/2}$; empty located Fe 2p$_{1/2}$). (b) Background-subtracted, *in situ* DRIFT spectra of the catalysts post their exposure to NH$_3$ (1000 ppm) at 50 °C. In (b), ***B*** and ***L*** denote catalytic Fe species with Brönsted and Lewis acid features (For interpretation of the references to colour in this figure legend, the reader is referred to the web version of this article).

composition was normalized with respect to its surface Fe composition. S500 showed ˜7.9 × 10^{-2} mol$_S$ mol$_{Fe}^{-1}$, which was larger than those of the other catalysts (*i.e.*, ≤ ˜6.7 × 10^{-2} mol$_S$ mol$_{Fe}^{-1}$). This suggested S500 surface included a considerable abundance of S-modified Fe species in comparison with the other catalysts.

XP spectra of S300-S600 were also inspected to determine which catalyst bored the most abundant surface SO$_4^{2-}$ species potentially used to yield SO$_4$·- (Fig. 4 (a)). Single broad peaks were observed throughout the S 2p regimes of the XP spectra and were fitted to two sub-bands with binding energies centered at 168.2–168.5 eV and 169.5–169.8 eV, respectively. These bands were assigned to surface SO$_3^{2-}$ and SO$_4^{2-}$ species inherent to the catalysts [15,50,53], among which S500 showed the greatest abundance of surface SO$_4^{2-}$ species (˜64.2% for S500; ≤ ˜56.9% for the others). In conjunction with the bulk S trend mentioned above, XP experiments also suggested S500 could accommodate the largest amount of SO$_4$·- species via radical transfer from ·OH to SO$_4^{2-}$. These also provided a compelling clue that SO$_4$·–assisted degradation of phenol could be most marked in S500.

Background-subtracted, *in situ* DRIFT experiments were also performed under such condition as to saturate pristine surface with SO$_2$ and O$_2$ at 300, 400, or 500 °C in order to simulate SO$_4^{2-}$-modified surfaces of S300, S400, or S500 (Fig. 4 (b)). It was reported covalent SO$_4^{2-}$ species could interact with the surface preferentially via *mono-*dentate configuration, whereas ionic SO$_4^{2-}$ analogues favor binding
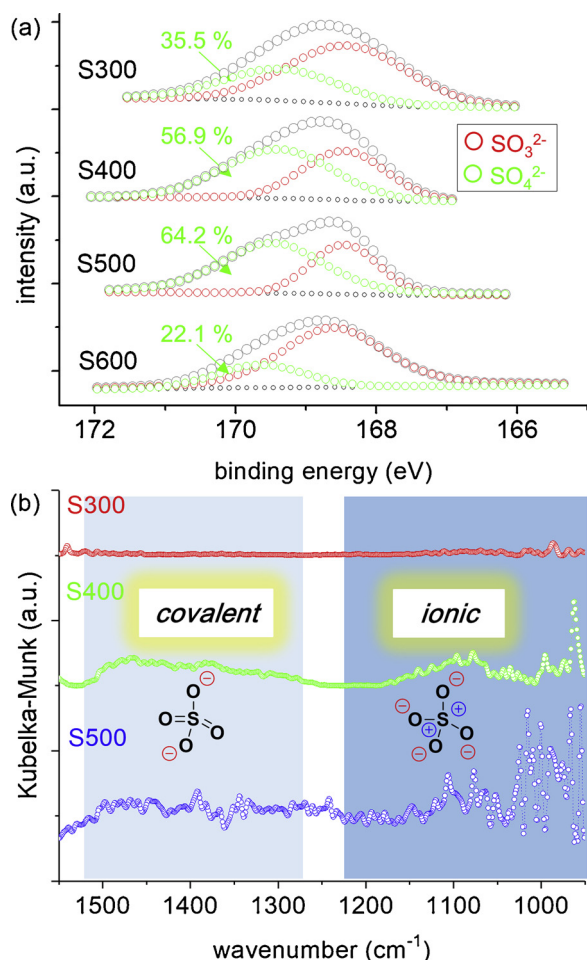
Fig. 4. (a) S 2p regions of XP spectra for the catalysts. In (a), grey, empty circles indicate fitted XP bands of the catalysts, wherein red and green circles indicate surface SO_3^{2-} and SO_4^{2-} species, respectively. (b) Background-subtracted, *in situ* DRIFT spectra of pristine post its exposure to SO_2 (1000 ppm) and O_2 (3 vol. %) at 300–500 °C. Bands observed in light blue and deep blue-shaded regimes result from SO_4^{2-}-modified Fe species with covalent and ionic character, respectively (For interpretation of the references to colour in this figure legend, the reader is referred to the web version of this article).

with the surface via *bi*-dentate configuration [54–56]. 300 °C was likely insufficient to populate SO_4^{2-} species on the surface of iron oxide and therefore barely showed bands in *in situ* DRIFT spectrum of iron oxide at 300 °C. This was in close line with the smallest surface S composition of S300 among all SO_4^{2-}-modified catalysts, as evidenced by their XP experiments. *In situ* DRIFT spectrum at 400 °C and 500 °C, however, showed bands at 1270-1550 cm^{-1} and 1000-1230 cm^{-1}, which indicated that the surfaces of S400 and S500 were populated by covalent SO_4^{2-} species and their ionic analogues [54–56]. This might likely justify that S600 surface also comprised of covalent and ionic SO_4^{2-} species. Noteworthy, the XP spectra of the catalysts suggested that the presence of SO_3^{2-} species on the surfaces of S300-S600 was indispensable, as was the case with SO_Y^{2-}-functionalized $Cu_3V_2O_8$ and $Fe_2V_4O_{13}$ on TiO_2 we reported previously [32,33]. However, the SO_4^{2-} binding configurations on the surfaces of the S400 and S500 led us to hypothesize that S500 can sustain $SO_4^{\cdot-}$-mediated phenol degradation performance better than that of S400. This was likely because SO_4^{2-} species rigidly bound to the iron oxide surface via *bi*-dentate configuration are more prevalent in the surface of the S500 in comparison with that of the S400.

3.2. H_2O_2 evolution and scission runs

Along with characterization experiments for exploring the surface features of the catalysts, we conducted reaction runs under controlled environments. (Specifics can be found in the Figure captions.) 3 V was selected as an electric potential for some of reaction runs because 3 V could enhance phenol degradation performance over a potential of 1–2 V (not shown). 3 V also aided in avoiding substantial liberation of the catalysts from the cathode, which was pronounced during reaction runs at 4 V or greater (not shown). We initially conducted electric potential-assisted H_2O_2 evolution runs in the presence of the catalysts (denoted as Control I) to obtain their H_2O_2 production profiles (mole of H_2O_2 evolved versus time). Electric conductivities of the reaction mixtures were also monitored during the first 2 h of the reaction runs because of the participation of e$^-$ in reducing O_2 (*i.e.*, $2H^+ + O_2 + 2e^- \rightarrow H_2O_2$ [24,26,27]). The primary objective of Control I runs was to look into the role of a specific catalyst in O_2 reduction, after which H_2O_2 was catalytically cleaved by $Fe^{\delta+}$ to produce $\cdot OH$.

For comparison with H_2O_2 evolution runs in the presence of the catalysts, we also performed two additional runs, wherein the catalyst or the binder used to coat the catalyst on the cathode was missing (blank or binder only). As shown in Fig. S1, the binder only run using only binder-coated (catalyst-uncoated) cathode showed slightly lower electric conductivities (~225 µS m^{-1}) than that (~240 µS m^{-1}) of blank run (without a binder and catalyst) or pristine run (with a binder and SO_4^{2-}-unmodified catalyst). However, the binder only run did provide H_2O_2 production profile comparable to those of the blank run and the pristine run (Fig. S1). These experiments could demonstrate that the binder used in this study played a minor role as 'electric resistor'. These therefore suggested that the binder could not hinder graphite or iron oxide-mediated transportation of e- to form H_2O_2 via O_2 reduction.

In addition, H_2O_2 evolution runs on the catalysts abruptly increased H_2O_2 quantities and saturated them within 10 min of the reaction runs (Fig. 5). We hypothesized '$Fe^{\delta+}$' species innate to the catalysts comprising of Fe_2O_3 or Fe_3O_4 can play a major catalytic role in accelerating H_2O_2 production'. It should be noted that Fe_3O_4 does incorporate greater amounts of $Fe^{\delta+}$ species than Fe_2O_3, as reported previously [15,57]. Catalytic O_2 reduction on Fe_3O_4-included materials, however, suffered from low H_2O_2 productivities [58–60]. Hence, it was highly likely that surface $Fe^{\delta+}$ species inherent the catalysts acted as minor species to direct H_2O_2 evolution.

Nonetheless, S400 and S500 outperformed the other catalysts in terms of H_2O_2 production. To clarify the major sources directing H_2O_2 generation, the amounts of O_2 dissolved in the reaction mixtures (N_{O2}) were measured during H_2O_2 evolution runs. The N_{O2} values prior to the reactions were 0.27 (± 0.02) mmol$_{O2}$ L^{-1} at 24.5 (± 0.7) °C, which
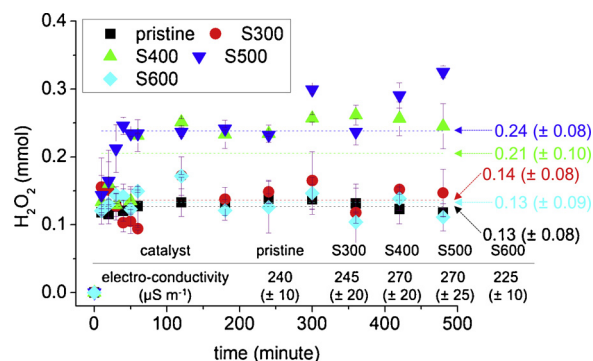

Fig. 5. Moles of H_2O_2 observed during H_2O_2 evolution runs in the presence of the catalysts (Control I). Dotted lines denote the averaged quantities of H_2O_2 monitored from 10 min to 8 h of reaction runs. Inset table showed averaged electro-conductivities of the reaction mixtures observed during the initial 2 h of reaction runs. Reaction condition: 0.2 g of catalyst; 0.2 mol of Na_2SO_4; 100 mL of de-ionized H_2O; 25 °C; 3 V.

was in close agreement with the quantity of saturated O_2 in H_2O reported elsewhere (~0.25 $mmol_{O2}$ L^{-1} at 25 °C) [61,62]. We then monitored the change in N_{O2} values during the reactions, throughout which the N_{O2} values were reduced by ~50% during the initial hour of the reactions and reached similar magnitudes. Interestingly, such reduced N_{O2} values during the reactions could be utilized to only yield ~0.1 $mmol_{H2O2}$ L^{-1} via O_2 reduction (i.e., $2H^+ + 2e- + O_2 \rightarrow H_2O_2$), which was far smaller than the quantities of saturated H_2O_2 observed during the H_2O_2 evolution runs on the catalysts (1.2–2.4 $mmol_{H2O2}$ L^{-1} in Fig. 5).

We conjectured that three plausible sources could compensate for the small amount of H_2O_2 evolved with the use of O_2 dissolved in H_2O. The 1st source could be O_2 species generated via H_2O oxidation on the graphite anode ($2H_2O \rightarrow O_2 + 4H^+ + 4e^-$) [28]. This might result in the formation of abundant O_2 species that moved to the cathode and were subsequently used to produce ~1.2 $mmol_{H2O2}$ L^{-1} via O_2 reduction. Of note, we could not observe the rapid increase in anodic H_2O oxidation-driven N_{O2} values during the initial period of the reaction runs. This might be due to the limitation of the O_2 detector used in this study, which did not allow for obtaining real-time N_{O2} profiles during the reactions. However, we did observe that the reaction runs on blank, pristine, S300, or S600 provided saturated H_2O_2 quantities of ~1.3 $mmol_{H2O2}$ L^{-1} within 5–10 min (Fig. 5). Hence, it was believed that H_2O_2 productions on the blank, pristine, S300, or S600 runs might proceed via rapid reaction dynamics, during which O_2 species generated via anodic H_2O oxidation could potentially function as major sources for H_2O_2 productions.

Again, O_2 species produced by anodic H_2O oxidation might be responsible for ~1.2 $mmol_{H2O2}$ L^{-1}, whose saturation was observed within 10 min of H_2O_2 evolution runs on the blank, pristine, S300, or S600. In contrast, the S400 and S500 runs saturated H_2O_2 quantities after an hour (Fig. 5). In addition, the S400 and S500 runs provided saturated H_2O_2 quantities of ~2.1 $mmol_{H2O2}$ L^{-1} and ~2.4 $mmol_{H2O2}$ L^{-1}, which left the O_2 sources of ~0.8 $mmol_{H2O2}$ L^{-1} and ~1.1 $mmol_{H2O2}$ L^{-1} unclarified. We postulated the 2nd source could be surface-mobile, labile oxygen (O_α) species present in the S400 and S500, which were reported to function as efficient oxygen donors for the excitation of C–H [63], C–O [64], N–H [65,66], or N–O bonds [67]. To evaluate the quantities of O_α species innate to all catalysts, O 1 s regimes of their XP spectra were analyzed (Fig. S2). As expected, the surfaces of the S400 and S500 were populated by far greater amounts of O_α species (O_α of $\geq$ ~42%) compared to the other catalysts (O_α of $\leq$ ~26%).

In addition to incorporating substantial amounts of O donors (O_α) used to potentially form H_2O_2 via O_2 reduction, the S400 and S500 might outperform the other catalysts in conveying e^- (the 3rd source) that could be also utilized to accelerate H_2O_2 formation. This could be partially corroborated by greater electric conductivities (~270 μS m^{-1}) of the reaction mixtures with the S400 or S500 in comparison with those with the other catalysts ($\leq$ ~245 μS m^{-1}). (See inset Table in Fig. 5.) All of these results suggested that the S400 and S500 could be desired for increasing ˙OH productivities.

We also performed H_2O_2 activation runs on the catalysts to examine their $Fe^{\delta+}$ species as catalytic H_2O_2 scissors to produce ˙OH (denoted as Control II). Control II runs were carried out under the identical conditions to those used for Control I runs except for the addition of H_2O_2 in the absence of an electric potential. To better simulate H_2O_2 scission performance of the catalysts, the amounts of H_2O_2 used for Control II runs were decided based on the saturated H_2O_2 quantities observed in Control I runs (i.e., ~0.13 mmol of H_2O_2 for pristine, S300, and S600; ~0.26 mmol of H_2O_2 for S400 and S500). To understand which catalyst could provide better consequences to cleave H_2O_2, their initial H_2O_2 activation rates ($-r_{H2O2, 0}$) were calculated. (Fig. S3; Details are found in Materials and Method section.) As shown in Fig. 6 (a), the S400 and S500 showed larger $-r_{H2O2, 0}$ values ($\geq$ ~1.1 μmol_{H2O2} g_{CAT}^{-1} min^{-1}) than the other catalysts ($\leq$ ~0.5 μmol_{H2O2} g_{CAT}^{-1} min^{-1}), which was in close agreement with the characterization results to quantify $Fe^{\delta+}$
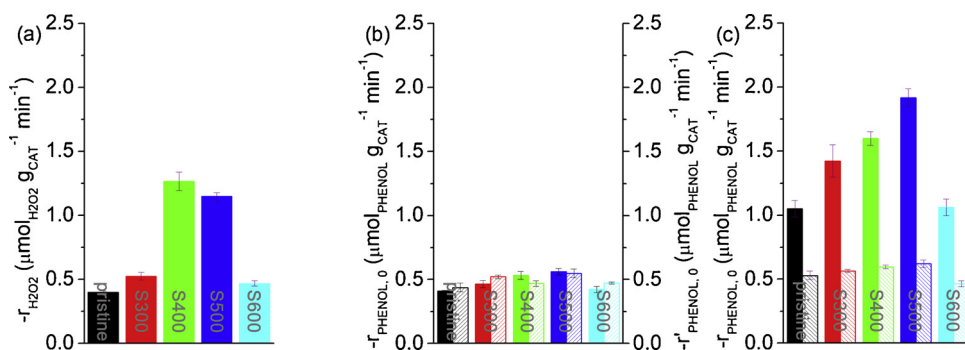
species innate to the catalysts, as shown in Fig. 3. Control I and II runs demonstrated that S400 and S500 were the preferred candidates for increasing H_2O_2 and ˙OH productivities.

3.3. Phenol decomposition runs

We then conducted a set of control runs, whose conditions were same as those utilized for Control II runs except for the addition of a recalcitrant model compound, phenol (denoted as Control III). The objective of Control III runs was to examine if ˙OH species produced via catalytic H_2O_2 cleavage on $Fe^{\delta+}$ species can dominate phenol decomposition. Initial phenol degradation rates of the catalysts ($-r_{PHENOL, 0}$) were also determined with the use of kinetic data shown in Fig. S4. (See how to calculate $-r_{PHENOL, 0}$ in Materials and Method section.) In the case of the pristine, S300, and S600, their $-r_{PHENOL, 0}$ values were in similar magnitudes of their $-r_{H2O2, 0}$ counterparts (0.4 − 0.5 $\mu mol_{H2O2 \text{ or}}$ $_{PHENOL}$ g_{CAT}^{-1} min^{-1}), as shown with filled rectangles in Fig. 6 (b). This might be reasonable when considering the quantities of H_2O_2 used during Control II runs on these catalysts (~0.13 mmol of H_2O_2) were similar to that of phenol used during Control III runs ($N_{PHENOL, 0}$ of 0.1 mmol). This was in contrast to the case of the S400 and S500, where their $-r_{PHENOL, 0}$ values (~0.5 μmol_{PHENOL} g_{CAT}^{-1} min^{-1}) decreased to half their $-r_{H2O2, 0}$ counterparts (~1.2 μmol_{H2O2} g_{CAT}^{-1} min^{-1}), despite the quantities of H_2O_2 used during Control II runs on these catalysts (~0.26 mmol of H_2O_2) were marginal in comparison with $N_{PHENOL, 0}$. (See filled rectangles in Fig. 6 (b).) Interestingly, $-r_{PHENOL, 0}$ values of Control III runs were similar to the initial phenol adsorption rates ($-r'_{PHENOL, 0}$) obtained via another set of control runs (denoted as Control IV in Fig. S5). The reaction conditions used for Control IV runs were identical to those used for Control III runs except for the elimination of H_2O_2 (˙OH precursor) from the reaction mixtures, thus allowing for the estimation of phenol adsorption kinetics on the catalyst surfaces. (See empty rectangles with diagonal lines in Fig. 6 (b).)

Of significance, Control I-II runs could justify the following statement that 'The generation of ˙OH via H_2O_2 scission on $Fe^{\delta+}$ species is highly likely and can depend on the kind of catalysts used.' Control III-IV runs could also rationalize the following statement that "˙OH can play a minor role in decomposing phenol, yet, may function as an activator to transform SO_4^{2-} functionalities on S300-S600 to $SO_4^{˙-}$ species.' Of additional significance, even with accepting two scientific deductions stated above, the following is still questionable: 'Why can we not observe significant degradation of phenol during Control III runs on S400 and S500, although these catalysts provide the largest compositions of surface $Fe^{\delta+}$ species (for ˙OH production), bulk S, and surface SO_4^{2-} species (for $SO_4^{˙-}$ production)?' It should be noted that Control II-IV runs were performed in the absence of an electric potential. As of now, we conjecture ˙OH has a short lifetime and therefore may remain challenging to fully radicalize SO_4^{2-} species, if the quantity of ˙OH located near the SO_4^{2-} functionalities is limited, as might be the case with Control III runs.

A feasible way to populate an abundant amount of ˙OH on or near the SO_4^{2-} functionalities can be the utilization of an electric potential, which may sustain H_2O oxidation (for O_2 production (*)) and catalytic H_2O_2 scission (for ˙OH production (*))/O_2 reduction (for H_2O_2 production (*)) on the anode and cathode, respectively [24,26,27]. We thus performed electric potential-assisted phenol degradation runs in the presence of the catalysts under conditions identical to those used for Control I runs except for the addition of phenol (denoted as Control V). One could claim that the quantities of H_2O_2 evolved during Control I runs were readily levelled-off and were transformed into a limited quantity of OH^-, thereby subsequently providing a limited amount of $SO_4^{˙-}$ functionalities used to degrade phenol during Control V runs. This hypothesis, however, could only be valid in the case, where $SO_4^{˙-}$ consumer (phenol) was missing in the reaction mixture. This was because '$H_2O_2 \leftrightarrow ˙OH \leftrightarrow SO_4^{˙-} \rightarrow$ phenol' pathway potentially inherent to our electric potential-assisted reaction system would strive to make up

Fig. 6. Initial reaction rates on the catalysts obtained during H_2O_2 activation ($-r_{H2O2,0}$ in (a), Control II), phenol degradation runs ($-r_{PHENOL,0}$ in (b) and (c)), or phenol adsorption runs ($-r'_{PHENOL,0}$ in (b)). In (b), filled rectangles indicate phenol degradation rates obtained in the presence of H_2O_2 ($-r_{PHENOL,0}$, Control III), whereas rectangles with diagonal lines indicate phenol adsorption rates obtained in the absence of H_2O_2 ($-r'_{PHENOL,0}$, Control IV). In (c), filled rectangles indicate rates obtained in the absence of *iso*-propyl alcohol (IPA, Control V), whereas rectangles with diagonal lines indicate rates obtained in the presence of IPA (Control VI). Reaction condition: 0.2 g of catalyst; 0.2 mol of Na_2SO_4; 100 mL of de-ionized H_2O; 0 mmol (a) or 0.1 mmol of phenol (b and c); 0.13 mmol (for pristine, S300, and S600) or 0.26 mmol of H_2O_2 (for S400 and S500) in (a) and (b); IPA of 0.24 mmol for pristine, 0.40 mmol for S300, 0.57 mmol for S400, 0.69 mmol for S500, and 0.24 mmol for S600 in.(c); 25 °C; 0 V (a and b) or 3 V (c).

for the loss of H_2O_2, $OH^•$, or $SO_4^{•-}$ upon the consumption of phenol by $SO_4^{•-}$. Such compensation might occur via three reactions marked with *, as mentioned above. As expected, the S400 and S500 enhanced phenol decomposition performance over the pristine, S300, and S600 in the presence of an electric potential. This was demonstrated by their phenol conversion profiles and $-r_{PHENOL,0}$ values (filled rectangles in Fig. 6 (c) and S6). This again could be primarily attributed by the largest compositions of surface $Fe^{\delta+}$ and SO_4^{2-} species innate to the S400 and S500, each of which could help promote productivities of $OH^•$ and $SO_4^{•-}$ via catalytic H_2O_2 scission and radical transfer from $OH^•$ to SO_4^{2-}, respectively. In addition, a change in pH from 7 to 4.3 or less during Control V runs on the S400 and S500 could cause the reaction of '$SO_4^{•-}$ + OH- → SO_4^{2-} + $OH^•$ (favorable under basic pH conditions [20,29–31])' to be of great favor in the opposite direction. Furthermore, large quantities of $OH^•$ and H^+ species generated during Control V runs on the S400 and S500 could reverse the reaction of '$SO_4^{•-}$ + H_2O → SO_4^{2-} + $OH^•$ + H^+'. All of our arguments supported the likelihood that $SO_4^{•-}$ derived from radical interconversion with $OH^•$ can direct phenol degradation, when SO_4^{2-}-functionalized iron oxide serves as a catalyst.

Although the reaction conditions seemed favorable to transfer radical from $OH^•$ to SO_4^{2-} for the generation of $SO_4^{•-}$, the significant $-r_{PHENOL,0}$ values of the S400 and S500 mediated by 'H_2O_2 ↔ $OH^•$ ↔ $SO_4^{•-}$ → phenol' pathway could be convincing only after ensuring that Control V runs were performed under a reaction-limited domain. For testing whether Control V runs were affected by diffusion, we chose the pristine because it can degrade phenol via 'H_2O_2 ↔ $OH^•$ → phenol' pathway. The S500 and S600 were also selected since the S500 and S600 provided the highest and the lowest $-r_{PHENOL,0}$ value among all SO_4^{2-}-modified iron oxides. Scanning electron microscopy images of these catalysts showed a broad spectrum of their particle sizes, most of which were < 50 μm (not shown). Hence, these catalysts were sieved to have different size of ≤ ~20 μm or 20–45 μm for the investigation of the internal diffusion effect on $-r_{PHENOL,0}$. In addition, reactions were performed at a greater stirring speed for the examination of the external diffusion effect on $-r_{PHENOL,0}$ (i.e., 400 rpm; 300 rpm employed for Control runs). Of note, the catalysts coated on cathode started to be detached at a stirring speed of 500 rpm and thus could not be tested at ≥ 500 rpm. The resulting $-r_{PHENOL,0}$ values of the pristine, S500, and S600 were almost constant even with the variation of the catalyst particles (See red and green columns in Fig. S8) or the stirring speeds (See red and blue columns in Fig. S8). This highly suggested that $-r_{PHENOL,0}$ values of these catalysts were not limited by internal/external diffusions and thus could be deemed as intrinsic activities.

3.4. Phenol degradation mediated by $SO_4^{•-}$ immobilized on iron oxide surface

We performed additional sets of control runs to provide concrete

evidence that '$SO_4^{•-}$ species supported on iron oxide can function as major sources to degrade phenol via heterogeneous catalysis.' The 1st set of control runs were carried out in the presence of a scavenging agent to quench both $OH^•$ and $SO_4^{•-}$ (i.e., *iso*-propyl alcohol denoted as IPA [68–71]) under the same conditions as those used to conduct electric potential-assisted phenol degradation (Control V) runs (denoted as Control VI in Fig. S9). The amounts of IPA used during Control VI runs were decided by counting all possible radical resources. For these determinations, two main hypothesis were formulated such that 1) 1 mol of H_2O_2 generated during Control I runs is cleaved to provide 2 mols of $OH^•$ at most and 2) 1 mol of bulk S innate to the catalyst constitutes of 1 mol of surface SO_4^{2-} species activated to form $SO_4^{•-}$. (See Fig. 6 caption.) As anticipated, Control VI runs showed $-r_{PHENOL,0}$ values that were far smaller than those obtained in Control V runs, where phenol was primarily degraded by $SO_4^{•-}$ (or $OH^•$) species. (See empty rectangles with diagonal lines in Fig. 6 (c).) In addition, the $-r_{PHENOL,0}$ values of the pristine, S300, and S600 approached the values obtained from their Control III and IV runs, both of which were mainly directed by the adsorption of phenol on their surfaces (Fig. 6 (b)). The S400 and S500, however, showed slightly larger $-r_{PHENOL,0}$ values than those obtained in their Control III and IV runs. In spite of adding the excessive amounts of the $OH^•$/$SO_4^{•-}$ quencher (IPA) into the reaction mixtures during Control VI runs, 'H_2O_2 ↔ $OH^•$ ↔ $SO_4^{•-}$ → phenol' pathway discussed above might be particularly accelerated on the S400 and S500 because of their abundant surface $Fe^{\delta+}$ and $SO_4^{•-}$ species. These scavenging runs, however, could be sound enough to argue that '$OH^•$ or $SO_4^{•-}$ radicals are the main phenol decomposers.'

The 2nd set of control runs were featured by the vacuum filtration of reaction mixtures and the sole change in the catalyst-coated cathodes to the catalyst-uncoated analogues post an hour of the reaction runs [15,38]. (denoted as Control VII; See grey-shaded regimes in Fig. 7.) These only left reaction filtrates that might contain leached, H_2O-soluble species to catalyze the production of $OH^•$ or leached $SO_4^{•-}$ used to degrade phenol via homogeneous catalysis [15,38]. We kept monitoring electric potential-assisted phenol degradation performance of the reaction filtrates in the presence of the bare anode and cathode [15,38]. The purpose of Control VII runs was to identify if the phenol degradation in the presence of an electric potential (Control V runs) is mainly directed by unsupported $Fe_{HOMO}^{\delta+}$ or SO_4^{2-} species with reaction pathways were shown in Fig. 1 [15,38]. All reaction filtrates were verified to contain 2.4–7.4 μmol of leached Fe species and consumed 180 (± 5) μmol of phenol over a reaction period ranging from 1 to 8 h. Such quantities of phenol consumed during Control VII runs, however, were similar to that of the blank run, where no catalyst was utilized (i.e., 175 (± 5) μmol). When considering phenol degradation on the blank run was primarily driven by anodic oxidation without the assistance of a catalyst [24,26,27], the leached Fe species could be thought of as insignificant sources to catalyze phenol degradation. Notably, the results of Control VII runs indicated that 'Electric potential-assisted
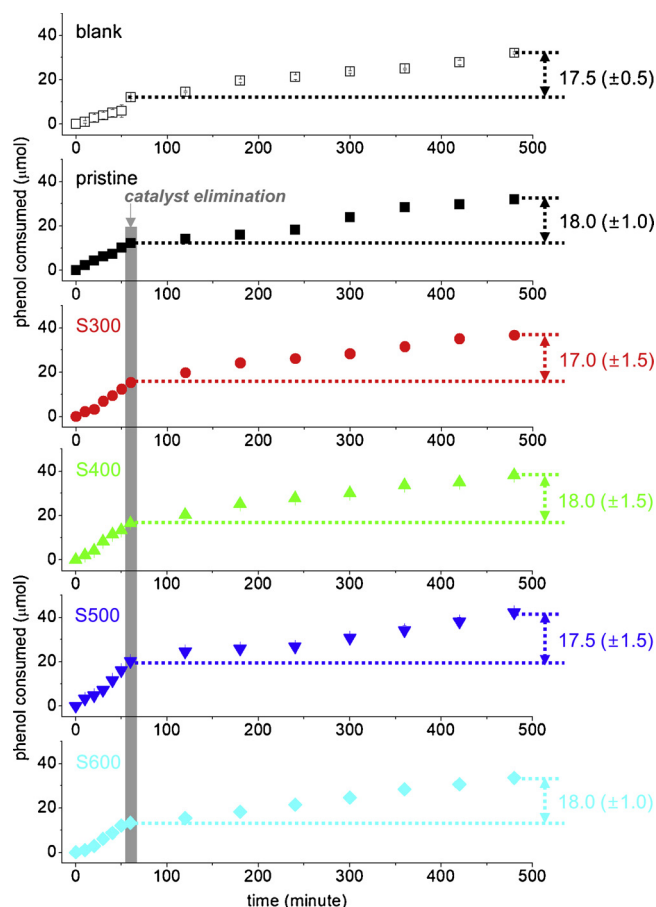
Fig. 7. Moles of phenol consumed during filtration runs in the absence (blank) or the presence of the catalysts (Control VII). Reaction condition: 0.2 g (or 0 g) of catalyst; 0.2 mol of Na_2SO_4; 100 mL of de-ionized H_2O; 0.1 mmol of phenol; 25 °C; 3 V.

phenol degradation (Control V) runs are mainly directed by supported $\cdot OH$ and $SO_4 \cdot^-$ species, where the production of each is mediated by $Fe^{\delta+}$ and SO_4^{2-} species deposited on the surface of iron oxide (i.e., $Fe_{HETERO}^{\delta+}$, $Fe_{ADD}^{\delta+}$, or $Fe\text{-}SO_4^{2-}$ shown in Fig. 1).'

Two control runs discussed above led us to conclude that 'Unleached $\cdot OH$ and $SO_4 \cdot^-$ species would play a pivotal role in accelerating phenol degradation.' The following question requires clarification: 'Which radical resource does act as the major decomposer of phenol?' To answer this question, we performed control runs to examine the recyclability of the catalysts (denoted as Control VIII). Recycle runs were performed under the identical conditions to those used for electric potential-assisted phenol degradation runs (Control V), whereas the catalysts post each of recycle runs were thoroughly rinsed, dried, accumulated, and coated for the next recycle run [15].

The S500 were chosen for these control runs because S500 showed the greatest phenol degradation performance among all catalysts during Control V runs, while providing the 2nd greatest quantities of CO-accessible $Fe^{\delta+}$ species (N_{CO}). If phenol degradation on S500 were dominated by heterogeneous catalytic $\cdot OH$ production on supported $Fe^{\delta+}$ species, one should observe that the trend in the $-r_{PHENOL, 0}$ values was in close agreement with the trend in the N_{CO} values during the recycle runs [15]. The S500 provided good recyclability to degrade phenol. This was supported by its $-r_{PHENOL, 0}$ values showing ~1.9 μmol_{PHENOL} g_{CAT}^{-1} min^{-1} for the 1st and 2nd cycles and ~1.6 μmol_{PHENOL} g_{CAT}^{-1} min^{-1} for the 3rd-5th cycles (Fig. 8 and S10). However, the trend in the $-r_{PHENOL, 0}$ values for the S500 was discrepant to the trend found in its N_{CO} values during each of the recycle runs, where the N_{CO} values were continuously reduced from ~2.6 μmol_{CO}
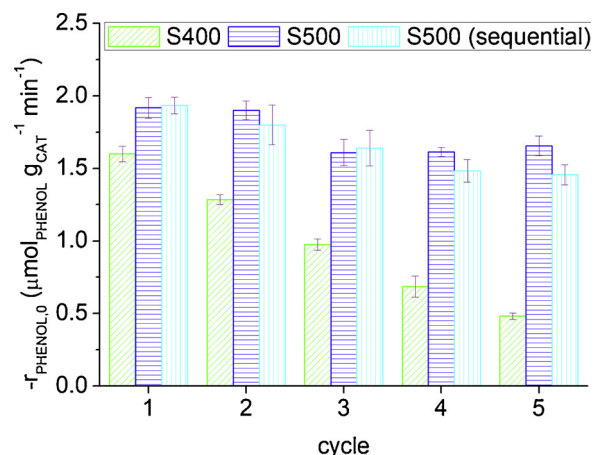

Fig. 8. Initial phenol degradation rates ($-r_{PHENOL,0}$) obtained during recycle runs in the presence of S400 or S500. S400 or S500 denotes the recycle run using the catalyst subjected to being rinsed, dried, accumulated, and re-coated on cathode prior to each of recycle runs (Control VIII). S500 (sequential) denotes the recycle run using S500 initially coated on cathode and only washed with the use of H_2O prior to each of recycle runs (Control IX). Reaction condition: 0.2 g of catalyst; 0.2 mol of Na_2SO_4; 100 mL of de-ionized H_2O; 0.1 mmol of phenol; 25 °C; 3 V.

g_{CAT}^{-1} (used for the 1st cycle) to ~0.2 μmol_{CO} g_{CAT}^{-1} (used for the 4th cycle). These experimental results provided one of decisive proofs that '$SO_4 \cdot^-$ species supported on iron oxide would be the primary decomposer of phenol.'

In addition, since the S400 also exhibited the 2nd greatest phenol degradation performance among the catalysts during Control V run, we also examined the recyclability of the S400 for its comparison with the recyclability of the S500. The S400 continuously reduced its phenol degradation consequences. This was demonstrated by its $-r_{PHENOL, 0}$ values that decreased from ~1.6 μmol_{PHENOL} g_{CAT}^{-1} min^{-1} to ~0.4 μmol_{PHENOL} g_{CAT}^{-1} min^{-1} during each of recycle runs (Fig. 8 and S10). At the same time, N_{CO} values of fresh and used S400 catalysts were initially ~0.9 μmol_{CO} g_{CAT}^{-1} (used for the 1st cycle), increased to ~1.6 μmol_{CO} g_{CAT}^{-1} (used for the 2nd cycle), and gradually decreased to ~0.3 μmol_{CO} g_{CAT}^{-1} (used for the 4th cycle). The change in the N_{CO} values of the fresh and used S400 catalysts was not in accordance with the trend in their $-r_{PHENOL, 0}$ values obtained during each of recycle runs. This again suggested that $\cdot OH$ producers (Fe^+ species) deposited on SO_Y^{2-}-modified iron oxide should not be the major active sites dominating phenol decomposition. Of note, the recycle experiments indicated 500 °C could be the preferred temperature for populating and rigidly dispersing SO_4^{2-} species on the surface of iron oxide, which could be converted to supported phenol consumers ($SO_4 \cdot^-$). This suggestion was also consistent to our hypothesis driven by SO_2-DRIFT experiments, as discussed above.

The S400 and S500 used for recycle runs were also characterized to diagnose their long-term stabilities. The S500 retained its bulk facets throughout the recycle runs, yet, gradually lost its crystallinity. This was validated by the XRD patterns of the used S500 catalysts, all of which exhibit persistent diffraction peaks corresponding to α-Fe_2O_3 with reduced intensities throughout the recycle runs (Fig. S11 (b)). To further ensure that such decrease in the crystallinity of the S500 could not affect its good recyclability in phenol degradation, we performed additional phenol degradation recycle runs on the S500. In contrast to the previous recycle runs on S500 discussed above (S500 in Fig. 8), these recycle runs served the S500 that was initially coated on cathode and consistently used it, while only washing the S500-coated cathode with H_2O after the completion of each of recycle runs (S500 (sequential) in Fig. 8). Two sets of recycle runs revealed comparable profiles of 'phenol conversion (X_{PHENOL}) versus time' (Fig. S10) as well as 'initial

phenol degradation rate ($-r_{PHENOL, 0}$) versus cycle' (Fig. 8). Of note, the S500 showed a gradual decrease in its X_{PHENOL} values during each of the recycle runs, partially resulting from the steady loss of its crystallinity (Fig. S11 (b)). However, despite the S500 decreased its $-r_{PHENOL, 0}$ values by ~0.3 μmol_{PHENOL} g_{CAT}^{-1} min^{-1} up to the 3rd cycle, the S500 retained its $-r_{PHENOL,0}$ values up to the 5th cycle (Fig. 8). This demonstrated that the S500 can exhibit good durability as a solid platform to sustainably convey supported SO_4^{2-} functionalities used to degrade phenol upon their excitation to produce supported $SO_4^{·-}$ species.

In contrast to the S500, the S400 suffered from severe structural collapse throughout the recycle runs, thereby revealing a near amorphous XRD pattern post the 5th cycle (Fig. S11 (a)). Additional characterizations were carried out to further contrast long-term stabilities of the S400 and S500. The amounts of S species leached from the surfaces of S400 or S500 during each of recycle runs could not be analyzed via inductively coupled plasma (ICP) because of the utilization of S-including Na_2SO_4 as an electrolyte. However, S500 consistently leached less Fe species (0.3 (± 0.1) mol. %) in comparison with S400 (0.9 (± 0.2) mol. %) throughout each of the recycle runs (analyzed via ICP), which again demonstrated that S500 enhanced chemical robustness over S400.

This was further supported by the comparison of bulk S quantities innate to as-synthesized and used catalysts via XRF analysis. The S500 maintained its original bulk S content of ~0.2 $mmol_S$ g_{CAT}^{-1} throughout the recycle runs. In contrast, the S400 with its original bulk S content of ~0.4 $mmol_S$ g_{CAT}^{-1} gradually lost its S species, thus revealing its bulk S quantities of ~0.1 $mmol_S$ g_{CAT}^{-1} and ~0.01 $mmol_S$ g_{CAT}^{-1} post the 3rd and the 5th cycle, respectively. The bulk S trends found in the S400 and S500 during the recycle runs were consistent with the trends in their surface S compositions (analyzed via XP spectroscopy). S500 showed 7.8 (± 0.1) $X10^{-2}$ mol_S mol_{Fe}^{-1} throughout its recycle runs, which was comparable to that prior to its reaction run (~7.9 × 10^{-2} mol_S mol_{Fe}^{-1}). S400, however, showed a continuous loss of its surface S species, as verified by its mol_S mol_{Fe}^{-1} values of ~5.6 × 10^{-2} mol_S mol_{Fe}^{-1} prior to the reaction run, ~ 0.8 × 10^{-2} mol_S mol_{Fe}^{-1} post the 3rd cycle, and ~0 mol_S mol_{Fe}^{-1} post the 5th cycle, respectively. These analyses suggested that S400 readily lost $SO_4^{·-}$ species active to degrade phenol and therefore kept losing its phenol decomposition efficiencies during each of the recycle runs. (See Fig. 8.)

For additional comparison, we inspected S 2p regimes of the XP spectra for the used S400 and S500 catalysts, all of which were deconvoluted into two sub-peaks corresponding to SO_3^{2-} and SO_4^{2-} species, as stated above. The S400 initially possessed relative abundance of surface SO_4^{2-} species as 56.9% prior to the reaction run and steadily decreased its SO_4^{2-} abundance to 23.2% post the 4th cycle (Fig. 4 (a) and 9 (a)). On the other hand, S500 possessed greater relative abundance of surface SO_4^{2-} species than those of S400 during each of the recycle runs such as 63.7 (± 0.5) % up to the 1st cycle and 43.0 (± 1.2) % up to the 4th cycle (Fig. 4(a) and 9 (b)). In conjunction with greater bulk and surface S contents of the S500 compared to those of the S400, these analyses suggested S500 was a preferred platform to firmly deposit SO_4^{2-} species on its surface over S400.

Importantly, the trends in surface SO_4^{2-} abundance observed in the used S400 and S500 catalysts were in close agreement with the trends in their initial phenol degradation rates during the recycle runs (Fig. 8 and 9). This again corroborated that phenol degradation performance of SO_4^{2-}-modified iron oxide could be mainly dominated by surface $SO_4^{·-}$ species. All of these results indeed demonstrated 500 °C would be the optimum temperature to maximize the quantity of $SO_4^{·-}$ precursors (SO_4^{2-}) firmly immobilized on the surface of iron oxide.

Of pivotal importance, for the quantification or surface $Fe^{\delta+}$ sites inherent to the catalysts (including S500), we used CO as a probe molecule because of its e^--abundant O atom that coordinates with e^--deficient, Lewis acidic $Fe^{\delta+}$ site [33,39,41]. Evaluating the numbers of Lewis acidic (L) sites present in the catalysts (i.e., $Fe^{\delta+}$), however, were apparently cumbersome because of the limited types of probe molecules

available to selectively quantify L sites. NH_3 was reported as another type of probe molecule for quantifying L sites via temperature-programmed desorption (TPD) [40,72–74]. However, the NH_3-TPD spectra of the catalysts usually provide a broad band, where strong Brönsted acid (B) sites and weak L sites are overlapped, thereby remaining difficult to be deconvoluted into B and L sites [75,76]. In addition, the quantification of L sites is substantially affected by the type of probe molecules. For instance, the amounts of NH_3-accessible B and L sites present in metal oxide catalysts are generally quantified as 1–50 $mmol_{NH3}$ g_{CAT}^{-1}, which are 10^2-10^3 times the amounts of CO-accessible L sites present in the identical catalysts [32,34]. To prove if $Fe^{\delta+}$ species were considerably populated on the surfaces of the recycled S500 catalysts (Control VIII), we employed complimentary characterization techniques to quantify their surface $Fe^{\delta+}$ species such as XP spectroscopy and background-subtracted, in situ NH_3-DRIFT spectroscopy under a NH_3 atmosphere at 50 °C. Large quantities of $Fe^{\delta+}$ species deposited on the surfaces of the used S500 catalysts were highly likely, as demonstrated by Fe 2p region of their XP spectra (Fig. 10 (a)). Albeit including a smaller quantity of $Fe^{\delta+}$ species in comparison with that of the S500 prior to the 1st cycle (~33 %), the S500 surface was significantly populated by $Fe^{\delta+}$ species prior to the 4th cycle (~ 20%). This was also in close line with the in situ DRIFT spectrum of S500 prior to the 4th cycle, which revealed considerable area under the peaks assigned to L sites (Fig. 10 (c)). Therefore, although the CO-accessible Lewis acidic $Fe^{\delta+}$ species present in the S500 seemed to be exhausted post a finite number of recycle runs (i.e., ~0.2 μmol_{CO} g_{CAT}^{-1} prior to the 4th cycle), Lewis acidic $Fe^{\delta+}$ species would not disappear in the S500 even after the S500 is significantly recycled to degrade phenol and could consistently help generate $^·OH$ species.

To present additional proof that supported $SO_4^{·-}$ species are the primary decomposer of phenol, we performed electric potential-assisted H_2O_2 evolution recycle runs on the S500 (denoted as Control IX) under the identical conditions to those of Control I runs except we rinsed, dried, accumulated, and coated S500 on the cathode post each of recycle runs (Fig. S12). Interestingly, the productivities of H_2O_2 were gradually reduced during each of recycle runs (~0.24 $mmol_{H2O2}$ g_{CAT}^{-1} for the 1st cycle → ~0.15 $mmol_{H2O2}$ g_{CAT}^{-1} for the 5th cycle). H_2O_2 productivities via '$2H^+ + 2e- + O_2 \rightarrow H_2O_2$' on the cathode could be potentially affected by three major O_2 sources such as O_2 dissolved in H_2O, O_2 produced from H_2O oxidation on the anode ($2H_2O \rightarrow O_2 + 4H^+ + 4e-$), or surface-labile O_α species present in the catalyst surface on the cathode, as suggested in Sub-section 3.2. The concentrations of dissolved O_2, however, remained constant throughout the recycle runs. Therefore, such a decrease in H_2O_2 productivities during the recycle runs might be partially ascribed to the continuous decrease in surface-labile O_α species innate to the S500, which could act as a precursor of H_2O_2 evolved during each of recycle runs. This could be partially validated by the XP spectra of the used S500 obtained during the phenol decomposition recycle runs (Control VIII), wherein relative abundance of O_α species innate to the S500 catalysts decreased from ~43% to ~27% up to the 3rd cycle (Fig. 10 (b)).

We then performed H_2O_2 activation recycle runs on the S500 (denoted as Control X) under the identical conditions to those of Control II runs. Again, these recycle runs were conducted in the absence of the electric potential, whereas the quantities of H_2O_2 used during each of recycle runs were determined according to the saturated H_2O_2 concentrations observed during Control IX runs (Fig. S13). Control X runs on S500 provided such an interesting trend in the initial H_2O_2 activation rate ($-r_{H2O2, 0}$) versus cycle, where the $-r_{H2O2, 0}$ values steadily decreased throughout the recycle runs (Fig. 11 (a)). Such a trend was also observed in the trend of N_{CO} values or surface $Fe^{\delta+}$ concentrations for the S500 catalysts recycled to decompose phenol in the presence of an electric potential (Control VIII; N_{CO} of 2.6 μmol_{CO} g_{CAT}^{-1} (used for the 1st cycle) → 0.2 μmol_{CO} g_{CAT}^{-1} (used for the 4th cycle); $Fe^{\delta+}$ of 32.6% (used for the 1st cycle) → 20.4% (used for the 4th cycle) in Fig. 10 (a)). This again could substantiate that '$^·$OH productivities are
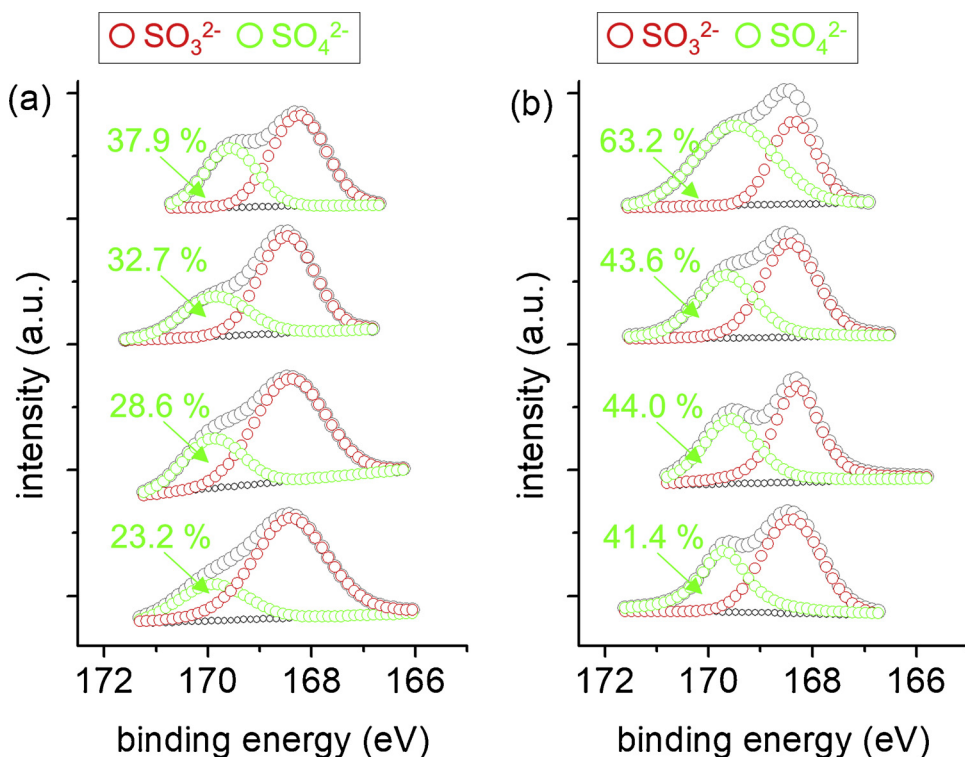
primarily mediated by the quantities of supported $Fe^{\delta+}$ species used to activate H_2O_2'. Of importance, the $-r_{PHENOL,\ 0}$ values for the S500 catalysts observed during phenol degradation recycle runs were greater than their corresponding $-r_{H2O2,\ 0}$ values observed during H_2O_2 activation recycle runs (Fig. 8 and 11 (a)). This again might be led by '$H_2O_2 \leftrightarrow \cdot OH \leftrightarrow SO_4^{\cdot-} \rightarrow$ phenol' route, potentially resulting in the continuous production of H_2O_2 species to compensate for the loss of $\cdot OH$ used to generate $SO_4^{\cdot-}$ during phenol degradation recycle runs in the presence of an electric potential (Control VIII). Of additional importance, the trend in the $-r_{H2O2,\ 0}$ values for the S500 kept decreasing during each of H_2O_2 activation recycle runs (Fig. 11 (a)). If phenol were mainly degraded by H_2O_2 activation-driven $\cdot OH$ species, one should observe the continuous reduction in the $-r_{PHENOL,0}$ values during each of the corresponding phenol degradation recycle runs. The $-r_{PHENOL,0}$ values for the S500 were reduced up to the 3rd cycle, yet, stayed under similar magnitudes throughout the rest of the cycles. (See blue columns in Fig. 8.) The trends in the $-r_{H2O2,0}$ and $-r_{PHENOL,0}$ values that were discrepant each other could verify that 'The supported $SO_4^{\cdot-}$ species are present in the S500 surface and act as the major crackers of phenol.' Although the recycle trend of the S500 in H_2O_2 activation could corroborate the role of the supported $SO_4^{\cdot-}$ species in phenol degradation (Fig. 11 (a)), such a role of $SO_4^{\cdot-}$ was still partially convincing.

A compelling way to verify the supported $SO_4^{\cdot-}$ present in SO_4^{2-}-functionalized iron oxides outweighs $\cdot OH$ in cracking phenol is to utilize various scavengers to quench $SO_4^{\cdot-}$ and $\cdot OH$ with distinct rates. Hence, we utilized *tert*-butyl alcohol (TBA), 1,4-dioxane, or tetrahydrofuran (THF) as an additional scavenger during electric potential-assisted phenol decomposition runs on the pristine and S500 (denoted as Control XI in Fig. S9). For fair comparison, the moles of TBA, 1,4-dioxane, or THF used during Control XI runs were set identical to those of IPA utilized during Control VI runs. Again, the selection of the pristine and S500 for Control XI runs was because they followed different pathway for generating radicals mainly used to degrade phenol (*i.e.*, '$H_2O_2 \leftrightarrow \cdot OH \rightarrow$ phenol' for pristine; '$H_2O_2 \leftrightarrow \cdot OH \leftrightarrow SO_4^{\cdot-} \rightarrow$ phenol' for S500).

TBA was reported to terminate $\cdot OH$ and $SO_4^{\cdot-}$ with the reaction rate constants of 3.8–7.6 × 10⁸ M⁻¹ sec⁻¹ ($k_{\cdot OH}$) and 4.0–9.1 × 10⁵ M⁻

¹ sec⁻¹ ($k_{SO4\cdot-}$), both of which were the smallest among those of the scavengers utilized in this study [22,70,71,77]. In addition, $k_{\cdot OH}$ values of the other scavengers increase in the following order of IPA (1.9 × 10⁹ M⁻¹ sec⁻¹) → 1,4-dioxane (3.1 × 10⁹ M⁻¹ sec⁻¹) → THF (4.0 × 10⁹ M⁻¹ sec⁻¹) [22,70,71,77]. These provided the basis of our prediction that the pristine could reveal $-r_{PHENOL,\ 0}$ values, among which $-r_{PHENOL,\ 0}$ upon the exposure to TBA was the greatest due to its smallest $k_{\cdot OH}$, whereas $-r_{PHENOL,\ 0}$ values in the presence of the other scavengers showed little difference due to their similar $k_{\cdot OH}$ magnitudes. $-r_{PHENOL,\ 0}$ values of the pristine, however, were anticipated to obey the trend in $k_{\cdot OH}$ values, thereby decreasing in the following order of IPA → 1,4-dioxane → THF. Control XI runs on the pristine provided $-r_{PHENOL,\ 0}$ values, whose trend was in close accordance to our predictions discussed above, while exhibiting the difference among $-r_{PHENOL,\ 0}$ values merely as < ˜0.09 $\mu mol_{PHENOL}\ g_{CAT}^{-1}\ min^{-1}$ (Fig. 11 (a)).

In the other hand, $k_{SO4\cdot-}$ values of the scavengers other than TBA increase in the following order of 1,4-dioxane (7.3 × 10⁷ M⁻¹ sec⁻¹) → IPA (8.2 × 10⁷ M⁻¹ sec⁻¹) → THF (2.8 × 10⁸ M⁻¹ sec⁻¹), yet, were far smaller than the corresponding $k_{\cdot OH}$ values [22,70,71,77]. Control XI runs on the S500 provided such $-r_{PHENOL,\ 0}$ values as to conform to the magnitudes of $k_{SO4\cdot-}$ values inherent to the scavengers, thereby decreasing $-r_{PHENOL,\ 0}$ values in the following order of TBA → 1,4-dioxane → IPA → THF. This might result from the accelerated termination of the supported $SO_4^{\cdot-}$ species on the S500 when using a scavenger with a greater $SO_4^{\cdot-}$ quenching rate. In addition, $-r_{PHENOL,\ 0}$ values of the S500 were consistently larger than those of the pristine upon the exposure to the identical scavenger, which could provide evidence that the supported $SO_4^{\cdot-}$ species primarily direct the phenol degradation on SO_4^{2-}-functionalized iron oxide (S500). Furthermore, $-r_{PHENOL,\ 0}$ values of the S500 differed by ˜0.25 $\mu mol_{PHENOL}\ g_{CAT}^{-1}\ min^{-1}$, which was about three times the difference of $-r_{PHENOL,\ 0}$ values of the pristine. This could result from the substantial difference of $k_{SO4\cdot-}$ values innate to the scavengers (10⁵-10⁸ M⁻¹ sec⁻¹) in comparison with the difference of their $k_{\cdot OH}$ counterparts (10⁸-10⁹ M⁻¹ sec⁻¹). This result could strongly corroborate that 'SO_4^{2-}-modified iron oxide facilitates phenol degradation with the primary use of the supported $SO_4^{\cdot-}$ species.'

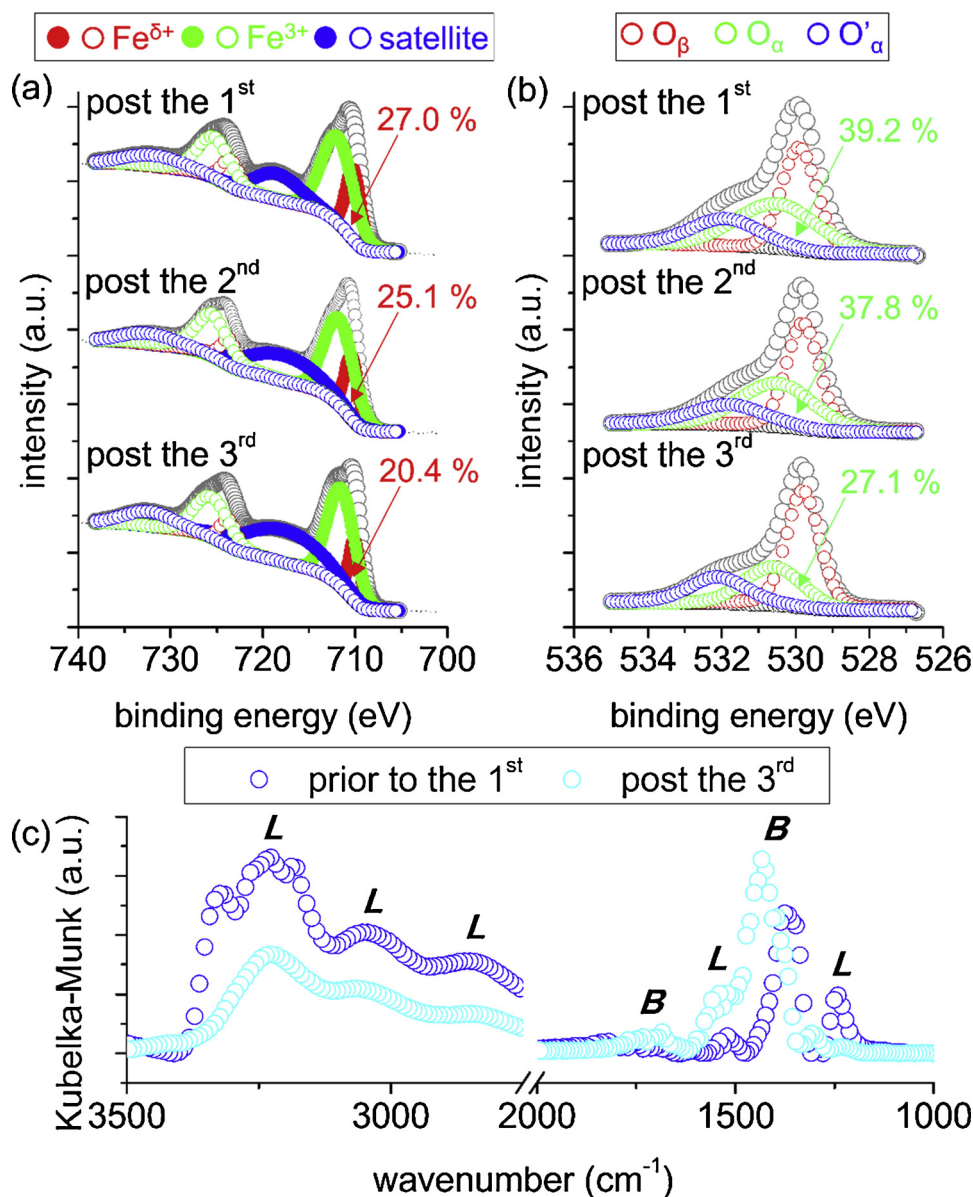Following all of our experimental validations on the supported

Fig. 10. (a) Fe 2p and (b) O 1 s regions of XP spectra for S500 collected post the 1st, the 2nd, and the 3rd recycle runs to degrade phenol (Control VIII). In (a), grey, empty circles indicate fitted XP bands of the catalysts, wherein circles indicate surface Fe species (filled located at Fe 2p $_{3/2}$; empty located Fe 2p $_{1/2}$). In (b), grey, empty circles indicate fitted XP bands of the catalysts, wherein empty circles indicate surface O species. (c) Background-subtracted, *in situ* DRIFT spectrum of S500 post the 3rd cycle after its exposure to NH$_3$ (1000 ppm) at 50 °C. *in situ* DRIFT spectrum of S500 prior to the 1st cycle post its saturation with NH$_3$ is also re-plotted for the reader's convenience. In (c), **B** and **L** denote catalytic Fe species with Brönsted and Lewis acid features. (For interpretation of the references to colour in this figure legend, the reader is referred to the web version of this article).

SO$_4^{\cdot-}$ species, we also contrasted thermal/electronic energies of SO$_4^{2-}$, SO$_4^{\cdot-}$, and their iron oxide-supported analogues via electronic structure calculations. The objective of this study was to answer the question of 'Can the reaction of 'SO$_4^{2-}$ + ·OH + H$^+$ → SO$_4^{\cdot-}$ + H$_2$O' or 'SO$_4^{2-}$ + ·OH → SO$_4^{\cdot-}$ + OH-' be feasible when SO$_4^{2-}$ species are supported by iron oxide?' For this study, we only considered the S500 surface (SO$_4^{2-}$ functionalities on Fe$_2$O$_3$) because of its outstanding phenol degradation efficiency relative to the others. The most common theoretical approach to simulate the inorganic (Fe$_2$O$_3$)-organic (SO$_4^{2-}$) interfaces is the periodic slab supercell approach, in which the organic molecule is deposited on the inorganic surface, whereas periodic boundary conditions are applied [78,79]. On the other hand, the cluster approach was reported to serve as an alternative to the slab supercell approach and is featured by isolating only a few metal oxide atoms (Fe$_2$O$_3$) to which an organic molecule (SO$_4^{2-}$) is bound [80,81]. We utilized the cluster approach because it can provide efficient and reliable evaluation of the Coulombic electron energy using local electronic wave functions and is particularly conducive to compute the charged organic molecules (*i.e.*, SO$_4^{\cdot-}$) [80,81]. Hence, it was anticipated that the cluster approach was sufficient enough for comparing the change in thermal/electronic energy involved during free (unsupported) SO$_4^{2-}$ →

free SO$_4^{\cdot-}$ ($\Delta E_{UNSUPPORTED}$) and supported SO$_4^{2-}$ → supported SO$_4^{\cdot-}$ ($\Delta E_{SUPPORTED}$).

The calculations provided $\Delta E_{UNSUPPORTED}$ as 147.2 kJ mol^{-1}, which was in close line with the literature resources arguing that the transition of SO$_4^{2-}$ to SO$_4^{\cdot-}$ via radical transfer from ·OH was considerably unfavorable [20,29–31]. Conversely, the calculations provided $\Delta E_{SUPPORTED}$ as -64.6 kJ mol^{-1}, which highly suggested that the radical transfer from ·OH to SO$_4^{2-}$ to produce SO$_4^{\cdot-}$ was greatly feasible when SO$_4^{2-}$ is supported by Fe$_2$O$_3$. Presumably, such remarkable change in ΔE values might be ascribed to the alteration of the binding character for the supported SO$_4^{2-}$ species upon their radicalization. The binding configuration of the supported SO$_4^{2-}$ species was *mono*-dentate with the Fe-O bond length of ~1.9 Å (Fig. 12 (a)). This was in good agreement with *in situ* SO$_2$-DRIFT spectrum of the catalyst at 500 °C, which also exhibited the *mono*-dentate (covalent) feature of the SO$_4^{2-}$ species bound to the iron oxide surface (Fig. 4 (b)). In contrast, the binding configuration of the supported SO$_4^{\cdot-}$ species was *tri*-dentate with the Fe-O bond lengths of ~2.3 Å (Fig. 12 (b)). Indeed, the supported SO$_4^{\cdot-}$ species were more energetically stable than the SO$_4^{2-}$ analogues. Nonetheless, in comparison with the supported SO$_4^{2-}$ species, the supported SO$_4^{\cdot-}$ counterparts were more distant from the Fe$_2$O$_3$ cluster and therefore were
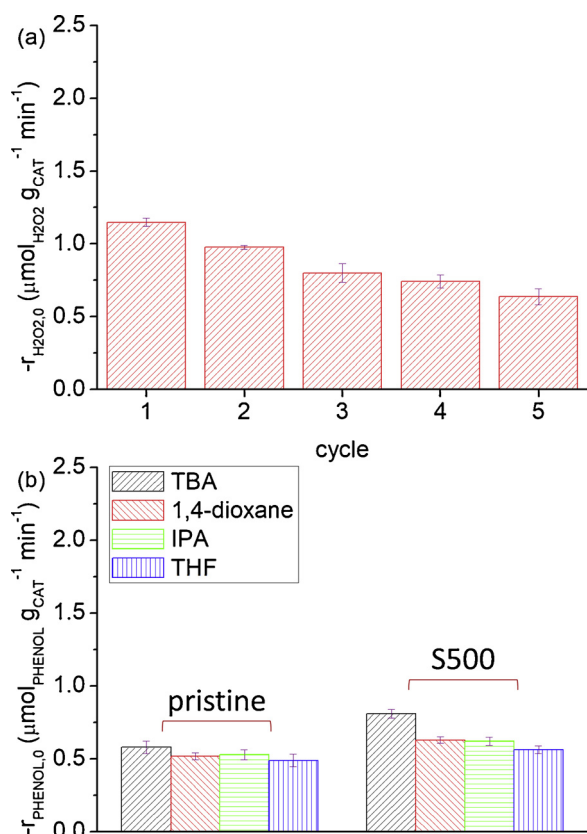
Fig. 11. (a) Initial H_2O_2 activation rates ($-r_{H2O2,0}$) on S500 obtained during its H_2O_2 scission recycle runs (Control X). (b) Initial phenol degradation rates ($-r_{PHENOL,0}$) obtained during electro-Fenton runs on pristine and S500 in the presence of a scavenging agent (*tert*-butyl alcohol (TBA), 1,4-dioxane, *iso*-propyl alcohol (IPA), or tetrahydrofuran (THF)) (Control XI). Reaction condition: 0.2 g of catalyst; 0.2 mol of Na_2SO_4; 100 mL of de-ionized H_2O; 0 mmol (a) or 0.1 mmol of phenol (b); 0.24 mmol of H_2O_2 for the 1st cycle, 0.22 mmol of H_2O_2 for the 2nd cycle, 0.20 mmol of H_2O_2 for the 3rd cycle, 0.17 mmol of H_2O_2 for the 4th cycle, 0.15 mmol of H_2O_2 for the 5th cycle (a), or 0 mmol of H_2O_2 (b); 0 mmol of the scavenger (a), 0.24 mmol of the scavenger for pristine, or 0.69 mmol of the scavenger for S500 (b); 25 °C; 0 V (a) or 3 V (b).
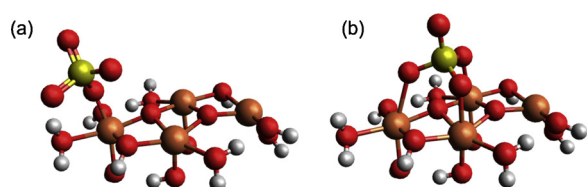

Fig. 12. Optimized structures for the supported SO_4^{2-} (a) and $SO_4^{\cdot-}$ species (b). SO_4^{2-} is bound to Fe_2O_3 cluster with the bond length of 1.897 Å, whereas $SO_4^{\cdot-}$ is bound to Fe_2O_3 cluster with the bond lengths of 2.17 Å, 2.196 Å, and 2.405 Å. Red, yellow, orange, and grey-colored ball indicate O, S, Fe, and H, respectively (For interpretation of the references to colour in this figure legend, the reader is referred to the web version of this article).

conjectured to vigorously interact with phenol to initiate its oxidative degradation. Although this study would highlight the significant potential of supported $SO_4^{\cdot-}$ in degrading aqueous contaminants, $SO_4^{\cdot-}$ species could be generated in the presence of an electric potential. The following critical question still remained: 'Can we produce supported $SO_4^{\cdot-}$ by feeding ·OH precursor (H_2O_2) into our reaction system in the absence of an electric potential?' The viability of radical transfer from ·OH to SO_4^{2-} with the use of H_2O_2 could be readily examined by comparing initial phenol removal rates among Control III ($-r_{PHENOL,0}$ via phenol degradation) and Control IV runs ($-r'_{PHENOL,0}$ via phenol

adsorption), whose values were found in Fig. 6. Again, Control III runs were performed under the identical conditions to those of electric potential-assisted phenol degradation runs (Control V) except H_2O_2 was used as an oxidant in the absence of electric potential. The amounts of H_2O_2 utilized during Control III runs were determined based on the saturated quantities of H_2O_2 observed during H_2O_2 evolution runs on the catalysts (Control I in Fig. 5). All catalysts showed initial phenol degradation rates ($-r_{PHENOL,0}$) of $0.4 - 0.5\ \mu mol_{PHENOL}\ g_{CAT}^{-1}\ min^{-1}$ during Control III runs. These $-r_{PHENOL,0}$ values were only about half or one third of the $-r_{PHENOL,0}$ values observed during Control V runs, where supported $SO_4^{\cdot-}$ species were populated with the help of abundant ·OH species generated upon H_2O_2 activation on the surface $Fe^{\delta+}$ species. In addition, the $-r_{PHENOL,0}$ values observed during Control III were also comparable to the initial phenol adsorption rates ($-r'_{PHENOL,0}$) obtained during Control IV runs on the identical catalysts, whose conditions were same as those of Control III runs except for the exclusion of H_2O_2 oxidant. All of these experimental results could indicate that the sole use of H_2O_2 in absence of an electric potential could not facilitate radical interconversion between ·OH and $SO_4^{\cdot-}$, unless a marginal amount of H_2O_2 was fed into SO_4^{2-}-functionalized iron oxides.

Furthermore, the increased efficiency of supported $SO_4^{\cdot-}$ over ·OH (generated by supported $Fe^{\delta+}$) as a phenol decomposer was highly convincing. This could be verified by a comparison of the $-r_{PHENOL,0}$ values among SO_4^{2-}-unmodified iron oxide (pristine) and SO_4^{2-}-modified analogues (S300-S600) during the electric potential-assisted phenol degradation runs (Control V). As shown in Fig. 6, the S300-S500 increased $-r_{PHENOL,0}$ values by factors ranging from 1.5 to 2 (1.5–2 $\mu mol_{PHENOL}\ g_{CAT}^{-1}\ min^{-1}$) compared to that of the pristine (~1 $\mu mol_{PHENOL}\ g_{CAT}^{-1}\ min^{-1}$). This highly suggested supported $SO_4^{\cdot-}$ outperformed ·OH in degrading phenol. Furthermore, electric potential-assisted runs on the S300-S500 (*i.e.*, electro-Fenton runs, Control V) also provided such $-r_{PHENOL,0}$ values that were three times the $-r_{PHENOL,0}$ values obtained during the generic Fenton runs on the identical catalysts (Control III). This could substantiate excellent efficacy of our reaction system over the generic Fenton reaction system. Overall, the SO_4^{2-}-functionalized Fe_2O_3 (S500) could greatly populate ·OH radical transfer-driven, supported $SO_4^{\cdot-}$ species, which provide good and recyclable performance for phenol degradation.

4. Conclusions

This is the 1st report with convincing proofs used to validate how to efficiently transfer radical from aqueous ·OH to surface SO_4^{2-}, leading to the formation of surface $SO_4^{\cdot-}$ available to degrade refractory pollutants (*e.g.*, phenol). We hypothesized such radical transfer could be pronounced under an electric potential-assisted condition to provide large quantity of H_2O_2 via O_2 reduction followed by catalytic H_2O_2 scission to form abundant ·OH species on a cathode. To verify our hypothesis, we employed porous iron oxide as a reservoir to highly and firmly disperse $Fe^{\delta+}$ and SO_4^{2-} species functioning as catalytic H_2O_2 scissors and $SO_4^{\cdot-}$ precursors, respectively. The distributions of $Fe^{\delta+}$ and SO_4^{2-} species inherent to iron oxide was readily altered by varying the temperatures (300–600 °C) used to functionalize iron oxide surface with the use of SO_2 and O_2. 500 °C was demonstrated as the optimum temperature to provide the greatest surface compositions of $Fe^{\delta+}$ and SO_4^{2-} species, thus facilitating 'H_2O_2 ↔ ·OH ↔ $SO_4^{\cdot-}$·' pathway better than the other temperatures. We also conjectured that the efficiency of our reaction system was primarily dominated by supported $SO_4^{\cdot-}$ radicals, which could decompose phenol via heterogeneous catalysis. Six sets of control runs provided sound evidence of our claim such as filtration runs to rationalize heterogeneous catalytic nature of radicals, recycle runs to convince $SO_4^{\cdot-}$ as the main catalytic site to degrade phenol, and scavenging runs to further justify $SO_4^{\cdot-}$ radicals as the major catalytic sites. Calculations of thermal/electronic energy change involved during the transition of supported SO_4^{2-} species to $SO_4^{\cdot-}$-analogues showed that the supported $SO_4^{\cdot-}$ species were more

energetically stable than SO_4^{2-} counterparts, thereby again warranting our claim of '$H_2O_2 \leftrightarrow \cdot OH \leftrightarrow SO_4 \cdot$-' pathway. Recycle runs and characterizations of the used catalysts also verified SO_4^{2-} functionalization at 500 °C could substantially populate ionic SO_4^{2-} species robustly bound to iron oxide surface via *bi*-dentate configuration, thereby helping maintain phenol degradation efficiency up to the 5th recycle run. This was in contrast to SO_4^{2-} functionalization at 400 °C that enabled to populate a relatively lesser amount of ionic SO_4^{2-} species on iron oxide surface, thus leading to a severe performance drop throughout the recycle runs. This study remarks the potential of aqueous OH^--driven, supported $SO_4 \cdot$- as a sustainable, effective decomposer of refractory contaminants.

Author contributions

Dr. J. Kim established the motivation and hypotheses for this work, designed experiments, refined/interpreted data, and drafted/revised the manuscript. Y. J. Choe performed experiments. Dr. S. H. Kim interpreted the data and provided comments on the original/revised manuscript. Dr. K. Jeong performed the computational works and provided comments on the revised manuscript.

Acknowledgements

Appendix A. Supplementary data

Supplementary material related to this article can be found, in the online version, at doi:https://doi.org/10.1016/j.apcatb.2019.04.015.

References

[1] S.O. Ganiyu, M. Zhou, C.A. Martínez-Huitle, Heterogeneous electro-Fenton and photoelectro-Fenton processes: a critical review of fundamental principles and application for water/wastewater treatment, Appl. Catal. B 235 (2018) 103–129.

[2] M. Antonopoulou, E. Evgenidou, D. Lambropoulou, I. Konstantinou, A review on advanced oxidation processes for the removal of taste and odor compounds from aqueous media, Water Res. 53 (2014) 215–234.

[3] A.D. Bokare, W. Choi, Review of iron-free Fenton-like systems for activating H_2O_2 in advanced oxidation processes, J. Hazard. Mater. 275 (2014) 121–135.

[4] C.K. Duesterberg, W.J. Cooper, T.D. Waite, Fenton-mediated oxidation in the presence and absence of oxygen, Environ. Sci. Technol. 39 (2005) 5052–5058.

[5] X. Li, S. Liu, D. Cao, R. Mao, X. Zhao, Synergetic activation of H_2O_2 by photogenerated electrons and cathodic Fenton reaction for enhanced self-driven photoelectrocatalytic degradation of organic pollutants, Appl. Catal. B 235 (2018) 1–8.

[6] S.B. Hammouda, F. Fourcade, A. Assadi, I. Soutrel, N. adhoum, A. Amrane, L. Monser, Effective heterogeneous electro-Fenton process for the degradation of a malodorous compound, indole, using iron loaded alginate beads as a reusable catalyst, Appl. Catal. B 182 (2016) 47–58.

[7] S.B. Hammouda, C. Salazar, F. Zhao, D.L. Ramasamy, E. Laklova, S. Iftekhar, I. Babu, M. Sillanpää, Efficient heterogeneous electro-Fenton incineration of a contaminant of emergent concern-cotinine- in aqueous medium using the magnetic double perovskite oxide Sr_2FeCuO_6 as a highly stable catalyst: degradation kinetics and oxidation products, Appl. Catal. B 240 (2019) 201–214.

[8] X. Xu, G. Pliego, A.L. Garcia-Costa, J.A. Zazo, S. Liu, J.A. Casas, J.J. Rodriguez, Cyclohexanoic acid breakdown by two-step persulfate and heterogeneous Fenton-like oxidation, Appl. Catal. B 232 (2018) 429–435.

[9] A.A. Oladipo, A.O. Ifebajo, M. Gazi, Magnetic LDH-based CoO–$NiFe_2O_4$ catalyst with enhanced performance and recyclability for efficient decolorization of azo dye via Fenton-like reactions, Appl. Catal. B 243 (2019) 243–252.

[10] M.A. Fontecha-Cámara, C. Moreno-Castilla, M.V. López-Ramón, M.A. Álvarez, Mixed iron oxides as Fenton catalysts for gallic acid removal from aqueous solutions, Appl. Catal. B 196 (2016) 207–215.

[11] X. Qian, M. Ren, M. Fang, M. Kan, D. Yue, Z. Bian, H. Li, J. Jia, Y. Zhao, Hydrophilic mesoporous carbon as iron(III)/(II) electron shuttle for visible light enhanced Fenton-like degradation of organic pollutants, Appl. Catal. B 231 (2018) 108–114.

[12] M. Pu, Y. Ma, J. Wan, Y. Wang, M. Huang, Y. Chen, Fe/S doped granular activated carbon as a highly active heterogeneous persulfate catalyst toward the degradation of Orange G and diethyl phthalate, J. Colloid Interface Sci. 418 (2014) 330–337.

[13] J. Du, J. Bao, X. Fu, C. Lu, S.H. Kim, Facile preparation of S/Fe composites as an effective peroxydisulfate activator for RhB degradation, Sep. Purif. Technol. 163 (2016) 145–152.

[14] J. Du, J. Bao, X. Fu, C. Lu, S.H. Kim, Mesoporous sulfur-modified iron oxide as an effective Fenton-like catalyst for degradation of bisphenol A, Appl. Catal. B 184 (2016) 132–141.

[15] Y.J. Choe, J.Y. Byun, S.H. Kim, J. Kim, Fe_3S_4/Fe_7S_8-promoted degradation of phenol via heterogeneous, catalytic H_2O_2 scission mediated by S-modified surface Fe^{2+} species, Appl. Catal. B 233 (2018) 272–280.

[16] L. Zhao, Y. Chen, Y. Liu, C. Luo, D. Wu, Enhanced degradation of chloramphenicol at alkaline conditions by S(-II) assisted heterogeneous Fenton-like reactions using pyrite, Chemosphere 188 (2017) 557–566.

[17] E.-J. Kim, J.-H. Kim, A.-M. Azad, Y.-S. Chang, Facile synthesis and characterization of Fe/FeS nanoparticles for environmental applications, ACS Appl. Mater. Interfaces 3 (2011) 1457–1462.

[18] L. Guo, F. Chen, X. Fan, W. Cai, J. Zhang, S-doped α-Fe_2O_3 as a highly active heterogeneous Fenton-like catalyst towards the degradation of acid orange 7 and phenol, Appl. Catal. B 96 (2010) 162–168.

[19] C. Liang, C.-F. Huang, Y.-J. Chen, Potential for activated persulfate degradation of BTEX contamination, Water Res. 42 (2008) 4091–4100.

[20] H. Liu, T.A. Bruton, W. Li, J.V. Buren, C. Prasse, F.M. Doyle, D.L. Sedlak, Oxidation of benzene by persulfate in the presence of Fe(III)- and Mn(IV)-Containing oxides: stoichiometric efficiency and transformation products, Environ. Sci. Technol. 50 (2016) 890–898.

[21] Y.-Y. Ahn, E.-T. Yun, J.-W. Seo, C. Lee, S.H. Kim, J.-H. Kim, J. Lee, Activation of peroxymonosulfate by surface-loaded noble metal nanoparticles for oxidative degradation of organic compounds, Environ. Sci. Technol. 50 (2016) 10187–10197.

[22] J. Du, J. Bao, Y. Liu, H. Ling, H. Zheng, S.H. Kim, D.D. Dionysiou, Efficient activation of peroxymonosulfate by magnetic Mn-MGO for degradation of bisphenol A, J. Hazard. Mater. 320 (2016) 150–159.

[23] J. Du, J. Bao, Y. Liu, S.H. Kim, D.D. Dionysiou, Facile preparation of porous Mn/Fe_3O_4 cubes as peroxymonosulfate activating catalyst for effective bisphenol A degradation, Chem. Eng. J. (2018).

[24] E. Brillas, I. Sirés, M.A. Oturan, Electro-fenton process and related electrochemical technologies based on Fenton's reaction chemistry, Chem. Rev. 109 (2009) 6570–6631.

[25] Y. Leng, W. Guo, X. Shi, Y. Li, A. Wang, F. Hao, L. Xing, Degradation of Rhodamine B by persulfate activated with Fe_3O_4: effect of polyhydroquinone serving as an electron shuttle, Chem. Eng. J. 240 (2014) 338–343.

[26] F.C. Moreira, R.A.R. Boaventura, E. Brillas, V.J.P. Vilar, Electrochemical advanced oxidation processes: a review on their application to synthetic and real wastewaters, Appl. Catal. B 202 (2017) 217–261.

[27] T.M. Do, J.Y. Byun, S.H. Kim, An electro-Fenton system using magnetite coated metallic foams as cathode for dye degradation, Catal. Today 295 (2017) 48–55.

[28] M. Panizza, G. Cerisola, Direct and mediated anodic oxidation of organic pollutants, Chem. Rev. 109 (2009) 6541–6569.

[29] D.E. Pennington, A. Haim, Stoichiometry and mechanism of the chromium(II)-peroxydisulfate reaction, J. Am. Chem. Soc. 90 (1968) 3700–3704.

[30] E. Hayon, A. Treinin, J. Wilf, Electronic spectra, photochemistry, and autoxidation mechanism of the sulfite-bisulfite-pyrosulfite systems. SO_2^-, SO_3^-, SO_4^-, and SO_5^- radicals, J. Am. Chem. Soc. 94 (1972) 47–57.

[31] C. Liang, H.-W. Su, Identification of sulfate and hydroxyl radicals in thermally activated persulfate, Ind. Eng. Chem. Res. 48 (2009) 5558–5562.

[32] J. Kim, D.W. Kwon, S. Lee, H.P. Ha, Exploration of surface properties of Sb-promoted copper vanadate catalysts for selective catalytic reduction of NO_x by NH_3, Appl. Catal. B 236 (2018) 314–325.

[33] J. Kim, D.H. Kim, D.W. Kwon, H.P. Ha, Rational selection of $Fe_2V_4O_{13}$ over $FeVO_4$ as a preferred active site on Sb-promoted TiO_2 for catalytic NO_x reduction with NH_3, Catal. Sci. Technol. 8 (2018) 4774–4787.

[34] J. Kim, S. Lee, D.W. Kwon, K.-Y. Lee, H.P. Ha, SO_3^{2-}/SO_4^{2-} functionalization-tailorable catalytic surface features of Sb-promoted $Cu_3V_2O_8$ on TiO_2 for selective catalytic reduction of NO_x with NH_3, Appl. Catal. A Gen. 570 (2019) 355–366.

[35] B. Tryba, A.W. Morawski, M. Inagaki, M. Toyoda, The kinetics of phenol decomposition under UV irradiation with and without H_2O_2 on TiO_2, Fe–TiO_2 and Fe–C–TiO_2 photocatalysts, Appl. Catal. B 63 (2006) 215–221.

[36] E. Mousset, L. Frunzo, G. Esposito, E.Dv. Hullebusch, N. Oturan, M.A. Oturan, A complete phenol oxidation pathway obtained during electro-Fenton treatment and validated by a kinetic model study, Appl. Catal. B 180 (2016) 189–198.

[37] J. Carbajo, A. Quintanilla, J.A. Casas, Assessment of carbon monoxide formation in Fenton oxidation process: the critical role of pollutant nature and operating conditions, Appl. Catal. B 232 (2018) 55–59.

[38] J. Kim, N.D. McNamara, J.C. Hicks, Catalytic activity and stability of carbon supported V oxides and carbides synthesized via pyrolysis of MIL-47 (V), Appl. Catal. A Gen. 517 (2016) 141–150.

[39] J. Kim, M.S. Abbott, D.B. Go, J.C. Hicks, Enhancing C–H bond activation of methane via temperature-controlled, catalyst–Plasma interactions, ACS Energy Lett. 1 (2016) 94–99.

[40] D.J. Rensel, J. Kim, V. Jain, Y. Bonita, N. Rai, J.C. Hicks, Composition-directed $Fe_xMo_{2-x}P$ bimetallic catalysts for hydrodeoxygenation reactions, Catal. Sci. Technol. 7 (2017) 1857–1867.

[41] J. Kim, D.B. Go, J.C. Hicks, Synergistic effects of plasma–catalyst interactions for CH_4 activation, Phys. Chem. Chem. Phys. 19 (2017) 13010–13021.

[42] K. Kosaka, H. Yamada, S. Matsui, S. Echigo, K. Shishida, Comparison among the Methods for Hydrogen Peroxide Measurements To Evaluate Advanced Oxidation Processes: Application of a Spectrophotometric Method Using Copper(II) Ion and 2,9-Dimethyl-1,10-phenanthroline, Environ. Sci. Technol. 32 (1998) 3821–3824.

[43] A. Adamescu, I.P. Hamilton, H.A. Al-Abadleh, Density functional theory calculations on the adsorption of monomethylarsonic acid onto hydrated iron (oxyhydr) oxide clusters, Comput. Theor. Chem. 1109 (2017) 58–63.

[44] A. Adamescu, I.P. Hamilton, H.A. Al-Abadleh, Density functional theory calculations on the complexation of p-Arsanilic acid with hydrated Iron oxide clusters: structures, reaction energies, and transition states, J. Phys. Chem. A 118 (2014) 5667–5679.

[45] S. Luo, Z. Wei, D.D. Dionysiou, R. Spinney, W.-P. Hu, L. Chai, Z. Yang, T. Ye, R. Xiao, Mechanistic insight into reactivity of sulfate radical with aromatic contaminants through single-electron transfer pathway, Chem. Eng. J. 327 (2017) 1056–1065.

[46] M. Krajewski, K. Brzozka, W.S. Lin, H.M. Lin, M. Tokarczyk, J. Borysiuk, G. Kowalski, D. Wasik, High temperature oxidation of iron–iron oxide core–shell nanowires composed of iron nanoparticles, Phys. Chem. Chem. Phys. 18 (2016) 3900–3909.

[47] M. Krajewski, W.S. Lin, H.M. Lin, M. Tokarczyk, S. Lewinska, N. Nedelko, A. Slawska-Waniewska, G. Kowalski, J. Borysiuk, D. Wasik, High temperature annealing of iron nanowires, Physica Status Solidi A Appl. Res. 212 (2015) 862–866.

[48] M. Lin, H.R. Tan, J.P.Y. Tan, S. Bai, Understanding the growth mechanism of α-Fe2O3 nanoparticles through a controlled shape transformation, J. Phys, Chem. C 117 (2013) 11242–11250.

[49] J. Liu, Z. Wu, Q. Tian, W. Wu, X. Xiao, Shape-controlled iron oxide nanocrystals: synthesis, magnetic properties and energy conversion applications, CrystEngComm 18 (2016) 6303–6326.

[50] W. Liu, Y. Wang, Z. Ai, L. Zhang, Hydrothermal synthesis of FeS2 as a high-efficiency fenton reagent to degrade alachlor via superoxide-mediated Fe(II)/Fe(III) cycle, ACS Appl. Mater. Interfaces 7 (2015) 28534–28544.

[51] S.O. Ganiyu, T.X. Huong Le, M. Bechelany, G. Esposito, E.D. van Hullebusch, M.A. Oturan, M. Cretin, A hierarchical CoFe-layered double hydroxide modified carbon-felt cathode for heterogeneous electro-Fenton process, J. Mater. Chem. A Mater. Energy Sustain. 5 (2017) 3655–3666.

[52] S.O. Ganiyu, T.X. Huong Le, M. Bechelany, N. Oturan, S. Papirio, G. Esposito, E. van Hullebusch, M. Cretin, M.A. Oturan, Electrochemical mineralization of sulfamethoxazole over wide pH range using FeIIFeIII LDH modified carbon felt cathode: degradation pathway, toxicity and reusability of the modified cathode, Chem. Eng. J. 350 (2018) 844–855.

[53] Y. Yu, J. Miao, J. Wang, C. He, J. Chen, Facile synthesis of CuSO4/TiO2 catalysts with superior activity and SO2 tolerance for NH3-SCR: physicochemical properties and reaction mechanism, Catal. Sci. Technol. 7 (2017) 1590–1601.

[54] S. Yang, Y. Guo, H. Chang, L. Ma, Y. Peng, Z. Qu, N. Yan, C. Wang, J. Li, Novel effect of SO2 on the SCR reaction over CeO2: mechanism and significance, Appl. Catal. B 136-137 (2013) 19–28.

[55] F. Liu, K. Asakura, H. He, W. Shan, X. Shi, C. Zhang, Influence of sulfation on iron titanate catalyst for the selective catalytic reduction of NOX with NH3, Appl. Catal. B 103 (2011) 369–377.

[56] M. Waqif, P. Bazin, O. Saur, J.C. Lavalley, G. Blanchard, O. Touret, Study of ceria sulfation, Appl. Catal. B 11 (1997) 193–205.

[57] J. Chun, H. Lee, S.-H. Lee, S.-W. Hong, J. Lee, C. Lee, J. Lee, Magnetite/mesocellular carbon foam as a magnetically recoverable fenton catalyst for removal of phenol and arsenic, Chemosphere 89 (2012) 1230–1237.

[58] W.R.P. Barros, Q. Wei, G. Zhang, S. Sun, M.R.V. Lanza, A.C. Tavares, Oxygen reduction to hydrogen peroxide on Fe3O4 nanoparticles supported on Printex carbon and Graphene, Electrochim. Acta 162 (2015) 263–270.

[59] Y. Ye, L. Kuai, B. Geng, A template-free route to a Fe3O4–Co3O4 yolk–shell nanostructure as a noble-metal free electrocatalyst for ORR in alkaline media, J. Mater. Chem. 22 (2012) 19132–19138.

[60] E.R. Vago, E.J. Calvo, Electrocatalysis of oxygen reduction at Fe3O4 oxide electrodes in alkaline solutions, J. Electroanal. Chem. Lausanne (Lausanne) 339 (1992) 41–67.

[61] A.O. Kondrakov, A.N. Ignatev, V.V. Lunin, F.H. Frimmel, S. Bräse, H. Horn, Roles of water and dissolved oxygen in photocatalytic generation of free OH radicals in aqueous TiO2 suspensions: an isotope labeling study, Appl. Catal. B 182 (2016) 424–430.

[62] T.E. Berger, Dissolved oxygen determination, J. Chem. Educ. 50 (1973) 160.

[63] W. Han, J. Deng, S. Xie, H. Yang, H. Dai, C.T. Au, Gold supported on Iron oxide nanodisk as efficient catalyst for the removal of toluene, Ind. Eng. Chem. Res. 53 (2014) 3486–3494.

[64] Q. Lin, C. Han, H. Su, L. Sun, T. Ishida, T. Honma, X. Sun, Y. Zheng, C. Qi, Remarkable enhancement of Fe–V–OX composite metal oxide to gold catalyst for CO oxidation in the simulated atmosphere of CO2 laser, RSC Adv. 7 (2017) 38780–38783.

[65] N. Apostolescu, B. Geiger, K. Hizbullah, M.T. Jan, S. Kureti, D. Reichert, F. Schott, W. Weisweiler, Selective catalytic reduction of nitrogen oxides by ammonia on iron oxide catalysts, Appl. Catal. B 62 (2006) 104–114.

[66] X. Mou, B. Zhang, Y. Li, L. Yao, X. Wei, D.S. Su, W. Shen, Rod-shaped Fe2O3 as an efficient catalyst for the selective reduction of nitrogen oxide by Ammonia, Angew. Chem. Int. Ed. 51 (2012) 2989–2993.

[67] G. Delahay, M. Mauvezin, B. Coq, S. Kieger, Selective catalytic reduction of nitrous oxide by Ammonia on Iron zeolite Beta catalysts in an oxygen rich atmosphere: effect of Iron contents, J. Catal. 202 (2001) 156–162.

[68] L. Wang, Aqueous organic dye discoloration induced by contact glow discharge electrolysis, J. Hazard. Mater. 171 (2009) 577–581.

[69] W.R. Haag, C.C.D. Yao, Rate constants for reaction of hydroxyl radicals with several drinking water contaminants, Environ. Sci. Technol. 26 (1992) 1005–1013.

[70] G.V. Buxton, C.L. Greenstock, W.P. Helman, A.B. Ross, Critical Review of rate constants for reactions of hydrated electrons, hydrogen atoms and hydroxyl radicals (˙OH/˙O−) in Aqueous Solution, J. Phys. Chem. Ref. Data 17 (1988) 513–886.

[71] R.E. Huie, C.L. Clifton, S.A. Kafafi, Rate constants for hydrogen abstraction reactions of the sulfate radical, SO4−: experimental and theoretical results for cyclic ethers, J. Phys. Chem. 95 (1991) 9336–9340.

[72] K.J. Lee, P.A. Kumar, M.S. Maqbool, K.N. Rao, K.H. Song, H.P. Ha, Ceria added Sb-V2O5/TiO2 catalysts for low temperature NH3 SCR: physico-chemical properties and catalytic activity, Appl. Catal. B 142-143 (2013) 705–717.

[73] D.W. Kwon, K.B. Nam, S.C. Hong, The role of ceria on the activity and SO2 resistance of catalysts for the selective catalytic reduction of NOX by NH3, Appl. Catal. B 166-167 (2015) 37–44.

[74] I. Song, S. Youn, H. Lee, S.G. Lee, S.J. Cho, D.H. Kim, Effects of microporous TiO2 support on the catalytic and structural properties of V2O5/microporous TiO2 for the selective catalytic reduction of NO by NH3, Appl. Catal. B 210 (2017) 421–431.

[75] F. Lónyi, J. Valyon, On the interpretation of the NH3-TPD patterns of H-ZSM-5 and H-mordenite, Microporous Mesoporous Mater. 47 (2001) 293–301.

[76] F. Hemmann, C. Jaeger, E. Kemnitz, Comparison of acidic site quantification methods for a series of nanoscopic aluminum hydroxide fluorides, RSC Adv. 4 (2014) 56900–56909.

[77] C.L. Clifton, R.E. Huie, Rate constants for hydrogen abstraction reactions of the sulfate radical, SO4−, Alcohols, Int. J. Chem. Kinet. 21 (1989) 677–687.

[78] J. Banerjee, S. Behnle, M.C.E. Galbraith, V. Settels, B. Engels, R. Tonner, R.F. Fink, Comparison of the periodic slab approach with the finite cluster description of metal–organic interfaces at the example of PTCDA on Ag(110), J. Comput. Chem. 39 (2018) 844–852.

[79] V.-A. Glezakou, L.X. Dang, B.P. McGrail, Spontaneous activation of CO2 and possible corrosion pathways on the low-index Iron surface Fe(100), J. Phys. Chem. C 113 (2009) 3691–3696.

[80] J. Hafner, Ab-initio simulations of materials using VASP: density-functional theory and beyond, J. Comput. Chem. 29 (2008) 2044–2078.

[81] P.S. Bagus, A. Wieckowski, C. Wöll, Ionic adsorbates on metal surfaces, Int. J. Quantum Chem. 110 (2010) 2844–2859.